Draft version June 27, 2017
Preprint typeset using LaTeX style emulateapj v. 01/23/15

SPECTROPOLARIMETRY OF HIGH REDSHIFT OBSCURED AND RED QUASARS

Rachael M. Alexandroff[1], Nadia L. Zakamska[1,2], Aaron Barth[3], Fred Hamann[4], Michael A. Strauss[5], Julian Krolik[1], Jenny E. Greene[5], Isabelle Pâris[7], Nicholas P. Ross[6]

Draft version June 27, 2017

ABSTRACT

Spectropolarimetry is a powerful technique that has provided critical support for the geometric unification model of local active galactic nuclei. In this paper, we present optical (rest-frame UV) Keck spectropolarimetry of five luminous obscured (Type 2) and extremely red quasars (ERQs) at $z \cong 2.5$. Three objects reach polarization fractions of $\gtrsim 10\%$ in the continuum. Though this is close to the theoretical maximum polarization fraction achievable from dust scattering at this wavelength range with typical dust distributions, this mechanism is still preferred because of the known scales of obscuration in these targets. Emission lines are polarized at a lower level than the continuum. This suggest that the emission-line region is on similar spatial scales as the scattering region. In three objects we detect an intriguing 90 degree swing in the polarization position angle as a function of line-of-sight velocity in the emission lines of Lyα, C IV and N V. We interpret this phenomenon using a conical emission line region and equatorial scattering model in which the scattering material is outflowing at several thousand km sec^{-1}. Our observations provide a tantalizing view of the inner region geometry and kinematics of high-redshift obscured and extremely red quasars and lend strong support for toroidal obscuration and powerful outflows on the scale of the emission line region, as previously indicated by near-infrared data.

Keywords: quasars: general – quasars: emission lines – polarization – scattering

1. INTRODUCTION

The classical unification model of Active Galactic Nuclei (AGN; Antonucci 1993; Urry & Padovani 1995) explains the difference between unobscured or "Type 1" AGN and obscured or "Type 2" AGN as the result of differences in viewing angle. In this model, a geometrically and optically thick torus of gas and dust surrounds the AGN accretion disk and broad-line region (BLR). Therefore, if the viewer's line of sight points through the torus, the majority of quasar emission from the accretion disk and the BLR in the optical, ultraviolet (UV) and soft X-rays is obscured. Such an obscured AGN is classified as a "Type 2" and is characterized at optical and ultraviolet wavelengths by little to no continuum emission and an absence of broad lines (e.g. Kauffmann et al. 2003; Hao et al. 2005). Quasars are high-luminosity AGN (typical bolometric luminosities $\gtrsim 10^{45}$ erg s^{-1}) and it was only in the last fifteen years or so that we have been able to identify appreciable numbers of Type 2 quasars and extend the unification model to all AGN luminosities (Norman et al. 2002; Stern et al. 2002; Zakamska et al. 2003; Stern et al. 2005; Reyes et al. 2008; Treister et al. 2009; Donley et al. 2012; Alexandroff et al. 2013; Yuan et al. 2016).

In the local universe, a convincing case for the geometric unification model was first made using optical spectropolarimetry of nearby Type 2 AGN (e.g. Antonucci & Miller 1985; Miller et al. 1991). Though the line of sight in Type 2 AGN is blocked by the obscuring torus, in this geometry optical AGN emission can still escape along the unobscured direction perpendicular to the torus and scatter off of free electrons or dust particles in the quasar host galaxy and into the observer's line of sight. This scattering causes the emission to become linearly polarized, making optical polarimetry and spectropolarimetry the best way to view this scattered emission from the nucleus (Miller & Goodrich 1990; Tran et al. 1995).

This process is also presumably occurring in unobscured or Type 1 AGN, but linearly polarized optical emission represents a much smaller fraction of the total light in these objects and the geometry is less favourable (e.g. Borguet et al. 2008). In fact, typical levels of polarization in unobscured AGN are only 0.5% (Berriman et al. 1990). In contrast, optical polarization levels in Type 2 quasars at low redshift can reach values of at least a few percent (Smith et al. 2002, 2003; Zakamska et al. 2005) and occasionally as high as $\gtrsim 20\%$ (Hines et al. 1995; Smith et al. 2000; Zakamska et al. 2005). In addition, light from the BLR scatters into our line of sight by the same process so the spectrum of a Type 2 AGN in polarized light possesses broad emission lines (e.g. Antonucci & Miller 1985; Zakamska et al. 2005). Thus, high measured levels of polarization and broad emission lines seen only in polarization are a tell-tale sign of obscured active nuclei in the classical orientation model. Indeed, it was imaging polarimetry and later deep spectropolarimetry that confirmed the presence of hidden AGN at the centers of radio galaxies– demonstrating that these ob-

Electronic address: rmalexan@jhu.edu
[1] Center for Astrophysical Sciences, Department of Physics and Astronomy, Johns Hopkins University, Baltimore, MD 21218, USA
[2] Deborah Lunder and Alan Ezekowitz Founders' Circle Member, Institute for Advanced Study, Einstein Dr., Princeton, NJ 08540, USA
[3] Department of Physics and Astronomy, University of California, Irvine, 4129 Frederick Reines Hall, Irvine, CA 92697, USA
[4] Department of Physics & Astronomy, University of California, Riverside, CA 92507, USA
[5] Department of Astrophysical Sciences, Princeton University, Princeton, NJ 08544, USA
[6] Institute for Astronomy, SUPA, University of Edinburgh, Royal Observatory, Edinburgh EH9 3HJ, UK
[7] Aix Marseille Université CNRS, LAM, (Laboratoire dAstrophysique de Marseille), Marseille, France

jects were in fact radio loud Type 2 AGN (see Tadhunter 2005, and references therein).

Few, if any, spectropolarimetric observations of radio-quiet obscured quasars at the peak of galaxy formation ($z \sim 2.5$) are available because until recently, such objects could not be readily identified. Furthermore, obscured quasars are by definition very faint at rest-frame optical and UV wavelengths, whereas spectropolarimetry requires high signal-to-noise ratio observations to detect polarized flux at the level of a few percent. Therefore, we can only perform polarimetry and especially spectropolarimetry of high-redshift obscured quasars with large telescopes and / or long integration times. Alexandroff et al. (2013) reported the results of spectropolarimetry performed on two high redshift ($z \sim 2.5$) rest-frame UV-selected Type 2 quasar candidates using the CCD spectropolarimeter (SPOL; Schmidt et al. 1992b) at the 6.5m MMT telescope. They demonstrated the presence of a polarization signature at the level of a few percent but low S/N and data on only two objects made further interpretation difficult.

While it is clear what the polarization signal is expected from a quasar obscured by a classical torus (Type 2), perhaps not all quasars possess a classical obscuring region. For example, Sanders et al. (1988) and Hopkins et al. (2006) argue that some obscured quasars may be a particular phase in quasar evolution after a merger or some other instability enshrouds the object in gas and dust. In this mode, obscuration exists on galaxy-wide scales. We then might expect a population of objects with nearly 4π steradians of obscuring material, where the openings in the obscured material are not well-organized in a conical structure. Red quasars at both low (e.g. Smith et al. 2000; Glikman et al. 2007; Urrutia et al. 2009; Glikman et al. 2012, 2013) and high (Eisenhardt et al. 2012; Wu et al. 2012; Tsai et al. 2015; Banerji et al. 2015; Ross et al. 2015; Hamann et al. 2017) redshift may be undergoing a phase of quasar evolution where the obscuring region exists on galaxy-wide scales as evidenced by the presence of galaxy-wide outflows (Zakamska et al. 2016) and merger signatures (Glikman et al. 2015). Such objects, would not have the same axial scattering regions, and thus would have a lower polarization fraction than classical Type 2 quasars. This work represents an attempt to identify such differences.

In this paper we present observations of five high redshift obscured and extremely red quasars (ERQs) with the Low Resolution Imaging Spectrometer (LRIS; Oke et al. 1995) in polarimetry mode (Goodrich et al. 1995). We describe our sample selection as well as observations and data reduction in Section § 2. Then Section § 3 describes our data analysis and results followed by a discussion of those results in Section § 4. We introduce our proposed model in Section § 4.1 and summarize our conclusions in Section § 5.

Throughout this paper, we adopt a cosmology with $h = 0.7$, $\Omega_m = 0.3$ and $\Omega_\Lambda = 0.7$. We use SDSS Jhhmm+ddmm notation throughout the text (full coordinates are listed in Table 1) with an additional marker letter to represent how the source was originally identified (see section 2.1 for more details). Throughout, u and q refer to Stokes flux densities while U and Q refer to percentages.

2. SAMPLE SELECTION, OBSERVATIONS AND DATA REDUCTION

2.1. *Parent Sample*

Our sample includes five reddened and obscured quasars selected by a variety of methods at redshift ($z \sim 2.5$) described in detail in Alexandroff et al. (2013), Ross et al. (2015) and Hamann et al. (2017). We briefly describe the original parent sample selection methods below. General information on these five quasars may be found in Table 1. The full sample was chosen to search for evidence of differences in the covering factor of obscuration (as traced by the polarization fraction) between these two populations.

Two of our sources, which we mark with a 'T' at the end of the designation, SDSSJ1515+1757T and SDSSJ1623+3122TE, were originally selected from the Sloan Digital Sky Survey (SDSS) Baryon Oscillation Spectroscopic Survey (BOSS; Dawson et al. 2013) by their narrow line widths (FWHM < 2000 km s^{-1} in both C IV and Lyman α) and weak continuum in the rest-frame UV, in an attempt to form an optically-selected sample of high redshift Type 2 quasars (for more details see Alexandroff et al. 2013). Only objects from Data Release 9 (Ahn et al. 2012) or earlier were included in this search, which yielded a sample of 145 Type 2 quasar candidates.

An additional three sources, labeled with an 'E', SDSSJ1232+0912E, SDSS1652+1728E and SDSSJ2215−0056E were selected based upon a combination of data from the SDSS and the Wide-Field Infrared Survey Explorer (WISE; Wright et al. 2010) AllWISE data release[8] to search for objects with red infrared-to-optical colours (Ross et al. 2015; Hamann et al. 2017). This selection method was used to search for obscured quasars at high redshift based on expected high infrared-to-optical ratios. A sub-sample of these very red objects show unusual spectroscopic properties including large rest equivalent width (REW) emission lines ($\gtrsim$ 100 Å), unusually high N V/Lyα ratios and emission lines with high kurtosis (lacking the typical broad wings of gaussian emission lines). These objects were labelled Extremely Red Quasars (ERQ). We separately selected objects with a required colour between the SDSS i-band and the WISE W3 band (12 μm) ≥ 4.6 and a measured REW of CIV > 100 Å, producing a final sample of 97 ERQs in a redshift range of $2.0 < z < 3.4$ (Hamann et al. 2017).

There is also some overlap between the two samples. While SDSSJ1652+1728E does not meet the strict cutoff required of the Alexandroff et al. (2013) sample of Type 2 candidates, its relatively narrow FWHM in C IV (< 2500 km s^{-1}) should be noted. Additionally, SDSSJ1623+3122TE is considered to be a part of the "expanded" sample of ERQs, defined to have "ERQ-like" line properties even if they are less red than the principal sample in $i - W3$ colours Hamann et al. (2017). We have labelled it as TE in table 1 to denote this joint classification. Both the Alexandroff et al. (2013) and the Ross et al. (2015), and Hamann et al. (2017) methods aim to select obscured quasars at high redshifts. While we still do not fully understand the physical properties

[8] http://irsa.ipac.caltech.edu/

of each of these populations, SDSSJ1623+3122TE and SDSSJ1652+1728E demonstrate that there can be some overlap between the methods.

2.2. *Rest-frame Optical Properties*

SDSS covers the rest-frame UV at the redshift of our objects and so follow-up near-infrared (NIR) spectroscopy is necessary to probe the rest-frame optical. We will study the rest-frame optical properties of our targets in more detail in forthcoming papers. For the purposes of the current study, we use the near-infrared (rest-frame optical) spectra primarily to distinguish between classical Type 1 and Type 2 objects, as well as ERQs.

The [O III]λ5007Å+Hβ spectra for all five targets studies in this Keck program are shown in Figure 1, with three objects on top from our new program on the Gemini Near-Infrared Spectrograph (GNIRS) on Gemini-North and two objects on the bottom from the previously published XShooter program (Zakamska et al. 2016). Our new GNIRS data was obtained in semester 15A in queue mode (PI Alexandroff). The instrument was operated in cross-dispersed mode using the 1/32 mm grating and with a slit width of 0.45″ to provide full wavelength coverage from 0.9 - 2.5 μm, which covers Hα, Hβ and [O III] in the rest-frame of our objects. Each object was observed in queue mode for a total of 60 minutes in a series of nodded 300s exposures along the slit. Data reduction was performed using the XDGNIRS package v2.0 (described in more detail in Mason et al. 2015), a wrapper script for the various PyRAF tasks in the Gemini IRAF package. The script was run in interactive mode and the data were examined at each step in the process to ensure that the pipeline was giving sensible results. As these objects are relatively faint point sources we manually set the position of the aperture for the trace of each order rather than having the program find it automatically.

Using the calibrated 1D spectra, we performed emission-line fits as in Zakamska et al. (2016). Briefly, [O III]λ4959Å and [O III]λ5007Å are always assumed to have the same velocity structure and a fixed flux density amplitude ratio of 0.337. Beyond this assumption, our fits are either "kinematically tied" – i.e., the same velocity structure is assumed for [O III], and Hβ – or "kinematically untied", in which Hβ has velocity structure which is different from [O III]. Our null hypothesis is that in Type 2 quasars, [O III] and Hβ are kinematically tied and their typical ratio is 10:1, with the caveat that both of these characteristics can be affected by strong outflows (Zakamska & Greene 2014; Zakamska et al. 2016).

Unlike low-redshift Type 2 quasars selected to have narrow Balmer lines, follow-up observations in the rest-frame optical (Greene et al. 2014) of twenty-five objects from our parent sample of Type 2 quasar candidates showed that $\sim$ 90% of objects displayed a broad Hα or Hβ line and all had intermediate values of extinction (0 mag $< A_{\rm v} <$ 2.2 mag) akin to Type 1.8/1.9 quasars. Yet, both SDSSJ1515+1757T and SDSSJ1623+3122TE – selected based on their narrow high-equivalent-width ultraviolet lines (Alexandroff et al. 2013) – show classical Type 2 quasar features in the optical: they have weak continua, narrow Hβ that has the same velocity structure as [O III], and [O III]/Hβ ratios of 9.9 and 6.9, respectively. These specific objects were chosen for spectropolarimetry follow-up because they are unambiguously high-redshift Type 2 quasars. SDSSJ1515+1757T shows no sign of [O III] outflows, whereas SDSSJ1623+3122T has a noticeable blue-shifted component in its [O III] emission.

SDSSJ1652+1728E has a mix of features. While it is best fit with a kinematically tied model with [O III]/Hβ=7.7, the rest-frame optical continuum is relatively stronger and marginally inconsistent with a Type 2 classification. In addition, the rest equivalent width of [O III]λ5007Å of 213Å is intermediate between Type 1s and Type 2s at these luminosities, Greene et al. 2014. This object shows very kinematically disturbed [O III], with the width containing 80% of line power of w_{80} = 1760 km sec^{-1}, which is in the upper $\sim$ 5% of [O III] velocity width in the $z < 1$ Type 2 population (Zakamska & Greene 2014). The remaining two targets, SDSSJ1232+0912E and SDSSJ2215−0056E, are ERQs. In the rest-frame optical, they have a mix of Type 2 and Type 1 characteristics as described in detail in Zakamska et al. (2016). Primarily, the rest-frame optical spectra is not best fit with a kinematically tied model (in the case of SDSSJ2215−0056E there is no preference between kinematically tied and untied) with REW of [O III]λ5007Å intermediate between expected Type 1 and Type 2 values. Both objects have extremely fast [O III] outflows– FWHM measured as 5630 and 360 km s^{-1} respectively. Such velocities are too large to be contained by any reasonable galaxy potential and perhaps indicate that these quasars are in the predicted "blowout" phase of quasar activity (Hopkins et al. 2006).

The sample of five objects was selected for follow-up with Keck LRISp to be either Type 2 objects in the rest-frame UV and optical or to be ERQs with signs of outflows. Thus, this sample allows us to probe the obscuring geometry and scattering efficiency over a variety of obscuring properties in quasars at high redshift.

2.3. *Observations and Data Reduction*

Data for this project were obtained as part of a NASA time allocation on the Keck Telescope in semester 2015A. All observations were conducted over the course of a single night (UT 2015-05-22) on Keck I from Keck Headquarters in Waimea in clear conditions with seeing around 0.6″. The observational setup was chosen to maximize S/N over resolution for our faint targets and to put the relevant emission lines of Lyα and C IV on the blue side CCD where cosmic ray (CR) effects could be minimized. We used a 1.0″ slit width and the D68 dichroic to separate light into blue and red beams. The blue side spectrograph used a 300 grooves mm^{-1} grism giving a dispersion of 1.43Å pixel^{-1} while the red side used a 400 grooves mm^{-1} grating which gave a dispersion of 1.16Å pixel^{-1}. This blue side grism provides some level of contamination on the red end due to second order light at $\lambda \gtrsim$ 6400 Å. No binning either spatially or spectrally was applied during observations. Combined wavelength coverage from both the blue and red sides stretched from 3100-10,300 Å, with a small overlap around $\sim$ 6500−6800 Å. Calibration darks, dome flats and arcs were taken the afternoon before the start of observations, with additional dome flats taken at the end of the evening.

Table 1: Basic properties of our obscured and highly reddened quasar targets for observation. Our targets span a range of properties in their line widths and colours. Position and redshift information from the SDSS Skyserver Data Release 12. C IV FWHM, REW and kt_{80} were measured by Hamann et al. (2017) for four objects. Measurements for SDSS1515+1757T are taken from the SDSS Skyserver Data Release 12. [O III] FWHM and luminosity are either from Zakamska et al. (2016) or derived from as yet unpublished data from Gemini North.

Short Name	RA	Dec	z	CIV FWHM	CIV REW	CIV kt_{80}	[OIII] FWHM	log $L_{[OIII]}$	i − W3	designation
	hh:mm:ss	dd:mm:ss		km s^{-1}	Å		km s^{-1}	erg s^{-1}	AB	
SDSSJ1232+0912E	12:32:41.73	+09:12:09.37	2.374	4787 ± 52	225 ±3	0.37	5627	43.92	6.8	ERQ
SDSSJ1515+1757T	15:15:44.00	+17:57:53.06	2.402	1118	67	–	856.4	43.98	2.0	T2
SDSSJ1623+3122TE	16:23:27.66	+31:22:04.29	2.344	1572±68	164±7	0.34	658.3	44.08	4.5	T2E
SDSSJ1652+1728E	16:52:02.64	+17:28:52.38	2.942	2403 ± 45	125 ± 2	0.33	1461	44.87	5.4	ERQ
SDSSJ2215−0056E	22:15:24.00	−00:56:43.80	2.493	4280 ± 112	153±5	0.37	3057	43.64	6.2	ERQ

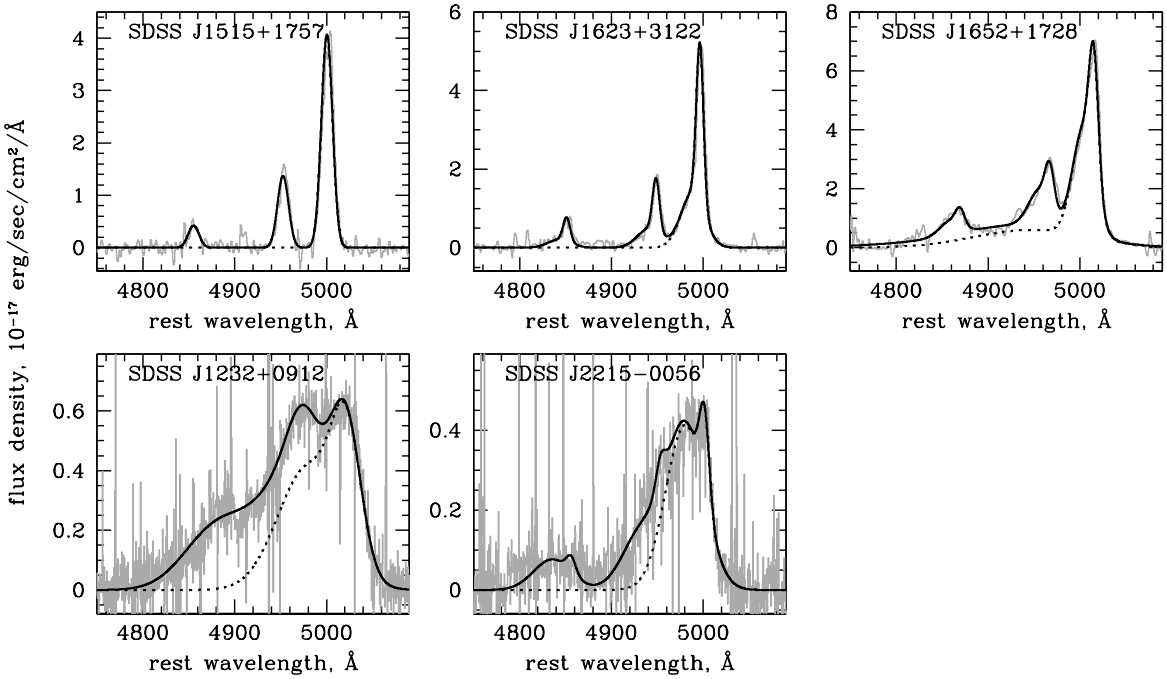

Figure 1. : The continuum-subtracted [O III]+Hβ complex and best fits for the five objects studied in this paper. Data was obtained for the top three objects with Gemini GNIRS and has not previously been published. Data for the bottom two objects was obtained with the VLT XShooter and was previously published in Zakamska et al. (2016). The grey histograms show the data, the solid black line shows the best overall fit and the dotted black line shows the [O III]λ5007Å fitted profile separately. In SDSSJ1515+1757T, SDSSJ1623+3122TE and SDSSJ1652+1728E the best fits are kinematically tied (i.e., [O III] and Hβ have the same velocity structure), and the best velocity fit is comprised of one, two and three Gaussian components, respectively. The best fits for SDSSJ1232+0913E and SDSSJ2215−0056E were previously presented in Zakamska et al. (2016) and are reproduced here. In SDSSJ1232+0913E, the best fit is kinematically untied; in SDSSJ2215−0056E it is kinematically tied; in both cases, two Gaussian components are used for [O III].

All of our science targets were observed in a standard sequence of four rotatable half-waveplate exposures (0°, 45°, 22.5°, and 67.5°) lasting 600 seconds on the blue side and 520 seconds on the red side to synchronize read-out times for the ends of the exposures. Four of the quasars were observed for two full observation sequences for a total observed time of 4800.0/4160.0 seconds on the blue and red sides respectively. SDSSJ2215−0056E was observed for a single full sequence– half the time of the other objects due to timing constraints. In addition, we observed the flux standard star Feige 34, the null (unpolarized) standard stars HD 109055 and BD+28°4211 (also a flux standard) and the polarized standards HD 155528 and HD 204827. All observations were done at the parallactic angle except for the special case of SDSS1652+1728E described further below.

Cosmic rays for the blue detectors are removed from the unreduced science images using the IRAF imaging version of L.A. cosmic (van Dokkum 2001). The red detectors, 300μm thick LBNL CCDs (Rockosi et al. 2010) have a much higher detection rate of CRs than the blue CCDs. Because each Stokes parameter is measured us-

ing four separate beam spectra and differencing pairs of spectra, any error in cleaning cosmic rays is multiplied four-fold for a single Stokes parameter, and eight-fold for the polarization fraction or polarization position angle. Thus, the red side CCDs suffer so acutely from cosmic ray contamination that the data were unusable.

Data reduction and calibration were conducted following the methods of Miller et al. (1988) and Barth et al. (1999). In brief, bias subtraction, flat fielding, spectral extraction, wavelength and flux calibration were first performed using IRAF, and polarization measurements were performed using routines written in IDL. Uncertainties due to photon-counting statistics and detector readout noise were propagated at every step of the reduction process, yielding error spectra for the Stokes parameters q and u. Extraction regions were 24 pixels (corresponding to $3.24''$) wide except for SDSS1652+1728E which had a different spatial profile (described below). The background region was calculated over 10 pixels (corresponding to $1.35''$) above and below the extraction region and additional 10 pixels away from the extraction region. A wide extraction region was used because the science targets were very faint.

SDSS1652+1728E is point-like in the SDSS images. There is another point-like source $1.6''$ away which doesn't have SDSS spectroscopy. During the observations, we placed the slit to cover both objects with the thought that the second object might be physically related. The spectra of this companion showed no features in the rest-frame UV and upon further inspection its SDSS photometric colours ($u-g=0.97$, $g-i=0.58$) place it firmly in the stellar locus for SDSS point-like objects (Yèche et al. 2010). The presence of this source on the slit makes proper extraction of SDSS1652+1728E complicated as the sources are so close as to be blended in the 2D spectra. We moved the background region an additional ten pixels away and made the extraction region only 20 pixels to avoid the additional source.

The extracted spectra were rebinned to 2Å bin^{-1} prior to polarimetry analysis. Then very fine wavelength alignment (to within 0.1Å) was done using the cross-correlation of all eight available extracted spectra for a single object. The zero point of the polarization angle was calibrated using one polarized standard star as a reference and the other as a check on our measured values. We find that calculated polarization values and angles for our polarized standards agreed well with published values. For HD204827, we measure a polarization of $5.760 \pm 0.003\%$ with a polarization position angle of $\theta = 59.48 \pm 0.02$ degrees in the B -band (4000-5000 Å). This is only 0.5% from the published values in Schmidt et al. (1992a). In addition, observations of unpolarized standard stars show well-behaved, flat response over the entire observed wavelength range and give a calculated polarization of 0.08%. Though this measurement is some combination of the stellar and instrumental polarization it is small enough that we conclude we can disregard the effects of instrumental polarization.

We conduct a variety of consistency checks with our data to convince us of the accuracy of our results. We measure the polarization for each sequence of exposures separately to make sure they were consistent before we combined them using a simple algorithm which weights each half equally. We also checked that the normal and optimal weighting algorithms (Horne 1986) for the source extraction gave similar results. We used the optimal weighting algorithm except for when measuring the line polarization for SDSS1515+1757T and SDSS1623+3122TE where the results did not agree well. It is also encouraging that clear detections of polarization in the continuum show consistent values of the observed polarization angle except in cases where the polarization angle can clearly be seen to physically vary as a function of wavelength (see section 3 for more information).

All polarization measurements were then made in the q and u spectra and converted to a debiased polarization and position angle, following the steps outlined in Miller et al. (1988). To increase S/N in the continuum we binned over several hundred Angstroms for each measurement. We are careful not to include wavelengths on the very red edge of the blue CCD to avoid the second order light due to the blue side grism. Polarization fractions and angles as well as the wavelength range over which each was calculated are listed in Table 2. The usual polarization is a positive-definite value, $p = \sqrt{q^2+u^2}$ which becomes problematic in our regime of low S/N so instead we report the debiased polarization which has a better behaved error distribution, $p = \sqrt{q^2+u^2-\sigma_q^2-\sigma_u^2}$. In the cases where measured error is larger than the measured signal we report a debiased polarization fraction of zero. The total flux spectra as well as continuum polarization and position angle measurements are shown in figure 2.

All our candidates lie at relatively high Galactic latitudes ($|b| > 30°$) with a range of $34.0° < |b| < 71.5°$, and thus the contribution to the polarization from interstellar dust is expected to be quite low. In fact, Serkowski et al. (1975) demonstrated that the Galactic interstellar polarization is measured to be $\lesssim 9\%$ E(B-V). We check the measured values of E(B-V) along the sightlines to our targets from both Schlegel et al. (1998) and Schlafly & Finkbeiner (2011) and find a range of values $0.0206 <$ E(B-V) < 0.1179 mag implying polarizations of $\lesssim 1\%$, much smaller than any of the values we are measuring in our targets. Thus we conclude that interstellar polarization has a negligible effect on our measured polarization values.

3. RESULTS

Our sample spans a range of rest-frame optical properties as described in Section 2.2, from classical Type 2 spectra with quiescent [O III] kinematics to extreme [O III] outflow activity. Here, we discuss the results of our spectropolarimetry analysis and connect them to other known multi-wavelength properties of our targets.

In Figure 2 we present the Keck LRISp data for each of our objects. We display the high sensitivity total UV spectrum followed by the binned polarization fraction and polarization position angle. We also display the full polarization position angle as a function of wavelength in the emission lines (smoothed using a least-squares polynomial smoothing filter with a window of five pixels) to allow variations to be apparent. In the following sections we discuss the observed trends in our spectra which we will attempt to connect to the relevant physics in section 4.

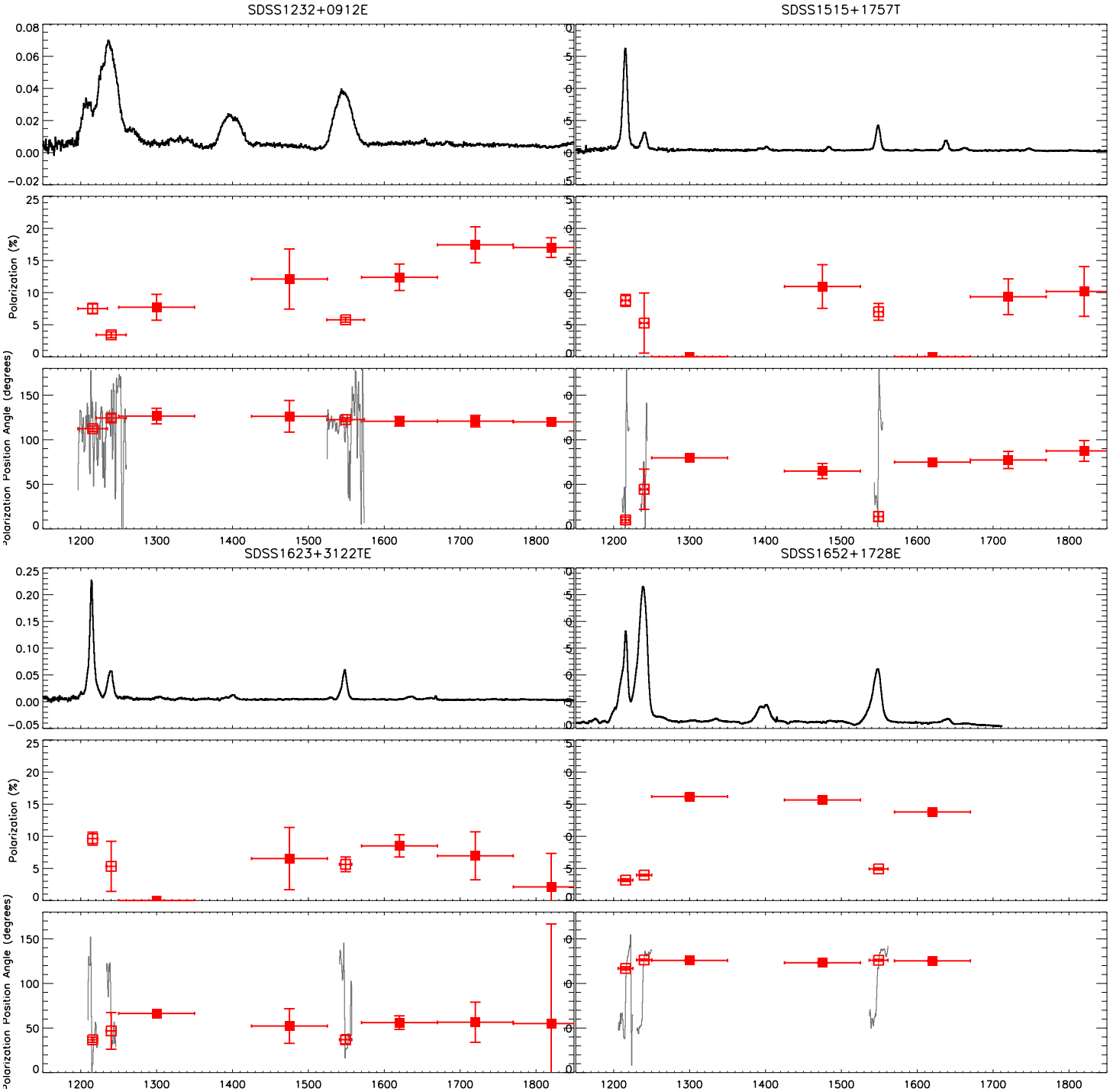

Figure 2. : LRISp spectra of our targets. The top panel shows the total flux spectrum while the middle panel shows the continuum polarization and statistical error in that measurement over the binned wavelength range indicated by the x-axis error bars (same as Table 2) and the bottom panel shows the same for polarization angle. The filled squares represent continuum measurements while the open squares represent emission line measurements. In grey, we include the unbinned polarization position angle in the emission lines to highlight the wavelength dependence. See section 3.4 for a discussion.

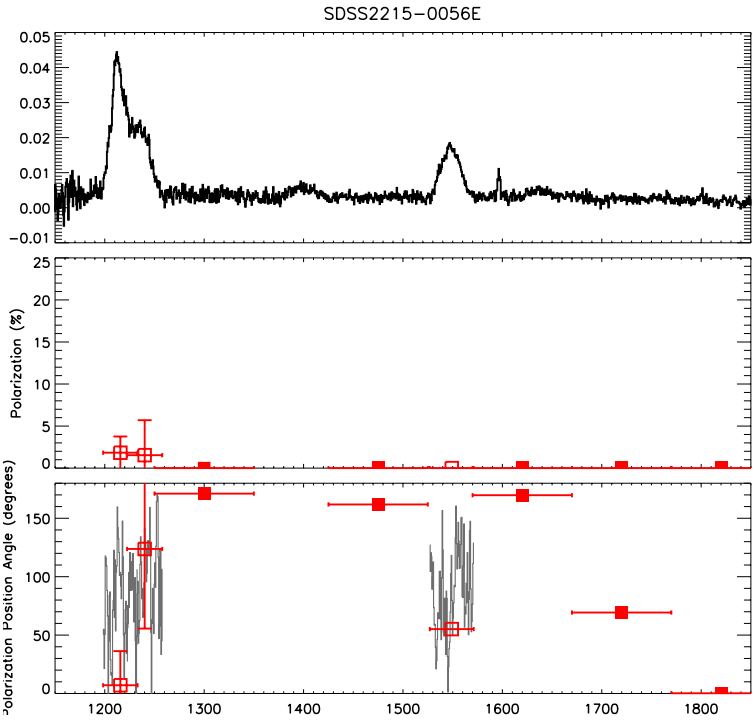

Figure 2. : continued

3.1. *Level of Continuum Polarization*

In Table 2 and Figure 2, we present continuum polarization measurements in several continuum regions, chosen in the rest-frame of the quasar to avoid contamination by UV emission lines. The level of continuum polarization just blueward of C IV (rest frame 1425Å-1525Å) spans from $15.7 \pm 0.4\%$ in SDSSJ1652+1728E to consistent with zero in SDSSJ2215−0056E.

These values of continuum polarization are very high for non-synchrotron emitting sources. The notable exception is SDSSJ2215−0056E, where we observe low levels of polarization with large uncertainty consistent with zero polarization in most wavelength ranges covered. Overall, the polarization values measured are much higher than that observed in Type 1 AGN where, for example, Berriman et al. (1990) found an average polarization of 0.5% for all 114 quasars from the Palomar-Green Bright Quasar Survey with a maximum polarization of 2.5%. These values are even on the extreme end of Type 2 AGN, radio galaxies and BAL quasars (Hines et al. 1995; Smith et al. 2000, 2002, 2003; Zakamska et al. 2005). For example, Smith et al. (2002) found no Type 2 quasars with polarization values $> 3\%$ but their continua were contaminated by host galaxy light. Zakamska et al. (2005) measure a polarization $> 3\%$ in nine of twelve Type 2 quasars and a mean polarization of 5.7% for all twelve objects with a maximum polarization of 15.4%. They contend all but one object are uncontaminated by the host galaxy though this is for the rest-frame optical (between ~ 2800 and ~ 6500Å). Smith et al. (2000) studied two Two Micron All-Sky Survey (2MASS)-selected obscured AGN and found continuum polarization values of $\sim 15\%$ in their optical continuum and BLR, in line with our measurements.

In Alexandroff et al. (2013), we found levels of polarization $> 5\%$ in the blue continuum of one object, SDSSJ220126.11+001231.5, and an overall average polarization of $1.9 \pm 0.3\%$, higher than could be accounted for by a typical unobscured quasar combined with instrumental systematics ($\lesssim 0.1\%$) and galactic polarization ($< 0.8\%$). The second object observed in that paper, SDSSJ004728.77+004020.3 had an average polarization of only $0.91 \pm 0.35\%$ making our interpretation of the nature of the source less clear. These objects however were not pre-selected to be unambiguous Type 2 quasars based on their rest-frame optical spectra unlike the objects designated with a 'T' in this work.

We argued in Alexandroff et al. (2013) that the continuum luminosity detected in our sample of high-redshift Type 2 candidates from SDSS was too high to be explained by the host galaxy alone. Instead, because the rest-frame UV slope was relatively flat or blue some sort of "patchy" geometry allowing some direct sightlines to the quasar or scattered light were required to make up a significant fraction of the observed continuum. Similarly, the high optical continuum in ERQs and other red quasars also suggests patchy obscuration or scattering (Assef et al. 2016; Zakamska et al. 2016; Hamann et al. 2017) though if the obscuring/scattering region is more or less spherically symmetric on galaxy scales then it would not lead to strong polarization. Detecting such high values of continuum polarization in these sources is unambiguous confirmation that most of the continuum emission is due to anisotropic scattered light.

In figure 3 we plot the mean continuum polarization fraction as a function of outflow velocity as measured by the [O III] w_{80} parameter. Type 2 and ERQ objects lie in different regions of this parameter space– the two Type 2s have the smallest outflow velocities. Though admittedly a small sample, we find no relationship between the rest-frame optical type (Type 2, ERQ) or the presence of [O III] outflows and the continuum polarization level.

3.2. *Wavelength Dependence of Continuum Polarization*

Scattering of the continuum can be due to dust or free electrons in the ionized gas. The expected polarization fraction due to electron scattering is described by the Thomson formula and is independent of wavelength. For dust scatting, the polarization fraction may vary as a function of wavelength depending on the dust composition and size distribution. Of course there are many complicating factors (see section 4.4), but it is still important to establish whether the polarization fraction varies in order to help determine the polarization mechanism.

There is marginal evidence for a wavelength-dependence in the polarization fraction in the continuum of our objects, with the polarization fraction appearing to rise at longer wavelengths. Such a trend is particularly evident in SDSSJ1232+0912E. Unfortunately, our achievable sensitivity makes it difficult to determine if this trend is real as most of the variation is within the observed error bars.

Alexandroff et al. (2013) also concluded for a single object that there was evidence for wavelength-dependent polarization fraction that was strongest at bluer wavelengths, the opposite of what we observe. A decreasing polarization fraction at redder wavelengths suggests either that the polarization is wavelength-dependent and

Table 2: Polarization percentages for each of our targets as a function of rest wavelength. All measurements are listed as percentage of the total flux. For emission lines the polarization was measured over the FWHM of C IV for each object.

Short Name	1250Å-1350Å	1425Å-1525Å	1550Å-1650Å	1650Å-1750Å	1750Å-1850Å	Lyα	N V	C IV
SDSSJ1232+0912E	7.7±2.0	12.1±4.7	12.4±2.1	17.4±2.8	17.0±1.5	7.5±0.8	3.4±0.5	5.8±0.4
SDSSJ1515+1757T	0.0	11.0±3.4	0.0	9.4±2.8	10.2±3.9	8.8±0.9	5.3±4.7	7.0±1.3
SDSSJ1623+3122TE	0.0	6.5±4.8	8.5±1.7	7.0±3.7	2.1±5.2	9.6±1.0	5.3±3.9	5.6±1.1
SDSSJ1652+1728E	16.2±0.3	15.7±0.4	13.8±0.3			3.2±0.2	4.0±0.1	4.9±0.2
SDSSJ2215−0056E	0.0	0.0	0.0	0.0	0.0	1.8±1.9	1.5±4.2	0.0

therefore likely caused by dust, or that the continuum is contaminated in this region by red unpolarized light that dilutes our polarization signal.

3.3. *Overall Polarization of Emission Lines*

The observed level of polarization in emission lines relative to the continuum is a good indicator of the geometry and polarization mechanism of the emission lines. In particular, the polarizing fraction of the emission lines relative to the continuum can indicate the scale of the scatterer. If the emitting region and the scattering region are on the same scale then this will dilute the polarization signature as there is no single, coherent scattering direction. Higher values of the ratio of emission line to continuum polarization imply scattering on large scales, beyond the line emitting regions, so that the lines remain as polarized as the continuum while lower values of this ratio imply that the scattering is on scales closer to or within the emission line region and thus the line emission is only marginally polarized. This geometric dilution in emission line regions relative to the continuum is found in many AGN sources (e.g. Stockman et al. 1981; Glenn et al. 1994; Goodrich & Miller 1995; Tran 1995) and implies that the scattering region is on a similar, or slightly larger scale, than the emission region.

We consider the UV emission lines of Lyα, N V and C IV, integrating over the FWHM of C IV (see Table 1). In all cases the observed polarization fractions are lower than the continuum polarization with the possible exception of the quasar SDSSJ1623+3122TE. Nevertheless, polarization values can still reach levels of $> 8\%$ in the Lyman α emission line, most notably in SDSSJ1515+1728T and SDSSJ1623+3122TE.

In figure 3 we plot the ratio of the line polarization fraction to the continuum polarization fraction just blueward of C IV between 1425Å and 1525Å. There is some evidence that those objects designated as classical Type 2s in our sample (left side of the plot, also with smaller outflow velocities), may show higher values of this ratio. In fact, the mean ratio over all lines is 0.36 for ERQs is while the mean ratio for Type 2 objects is 0.85. In a scenario where resonant scattering has little effect on the measured polarization fraction this ratio measures the geometric mixing of each emission region and the scattering medium. This implies that the scattering regions for classical Type 2s may be on larger scales than the scattering regions in ERQs. This scenario is complicated if resonant scattering has a strong effect on the measured emission line polarization fractions but, in section § 4.4 we consider and reject the possibility of resonant scattering as the source of polarization in the emission lines of our objects.

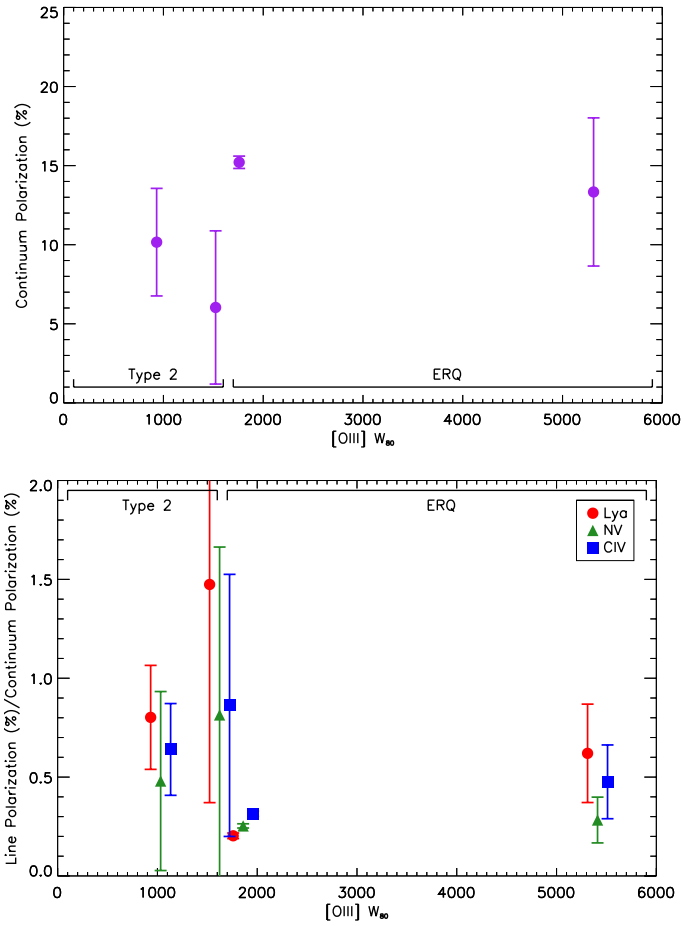

Figure 3. : **Top:** Continuum polarization levels (percent) averaged over the continuum regions as a function of outflow speed as measured by the w_{80} parameter of [O III]. We see no trend between this measure of the outflow speed and the polarization fraction in the continuum. **Bottom:** Ratio of line polarization for the three prominent lines in the observable range of our objects to continuum polarization levels measured blueward of C IV between 1425Å and 1525Å (percent) as a function of outflow speed as measured by the w_{80} parameter of [O III]. There is some evidence that the Type 2 objects are in a different regime with higher line polarizations. In a scenario where this ratio is a measure of the geometric mixing of the emission and scattering regions this would imply that the scattering regions in classical Type 2s are on larger scales than the scattering regions of ERQs.

3.4. *Kinematics of Line Polarization*

There is also a significant amount of variation in the polarization fraction across emission lines. The polarization fraction tends to reach a minimum around the line centroid and a maximum at a redshift between $+1000 < v_{max} + 2000$km s^{-1}. This pattern is perhaps most pronounced in SDSSJ1652+1728E (Fig. 4). Such wavelength-dependent polarization in emission lines is present in several objects in our sample and may provide a unique window in to our understanding of the scattering geometry. We discuss further in section § 4.

Perhaps the most intriguing trend we observe is the wavelength-dependence of the polarization position angle across all emission lines in many of our objects. This trend can be observed in SDSSJ1515+1728T, SDSSJ1623+3122T and most dramatically in SDSSJ1652+1728E. This observed trend has several key features. First, the polarization position angle appears to vary by almost exactly $\pi/2$ radians across the emission line (again, see Fig. 4). Most notably for our analysis, the polarization position angle of the continuum is the same as the polarization position angle of the emission line gas at the reddest wavelengths. This trend can easily be observed in Figure 4 but we also present the observation as a change in the ratio of the u and q Stokes parameters in Figure 5. This format is inspired by similar figures for the study of polarization in supernovae (SNe; for a thorough review see Wang & Wheeler 2008).

If there were a single, smooth and axisymmetric scattering region where the polarization was independent of wavelength, we would find a consistent polarization fraction which would result in a clustering of all data points in the Q/U plane. If, instead, there is some form of homologous expansion of the scattering material ($v \propto r$), then at each wavelength the viewer is seeing a different slice or shell in the expanding scattering material. Each slice will have a different optical depth which would introduce a wavelength dependence to the polarization and thus cause the data points to spread out in a line in the Q/U plane, also known as the "dominant axis" (Hoeflich et al. 1996; Wang et al. 2001). Deviations from this straight line in the Q/U plane then represent deviations from the assumptions of smoothness or axisymmetry in the scattering geometry. These deviations must be finite to maintain the presence of a single dominant axis in the plane (e.g. the presence of clumpy material). This model ignores scattering in the interstellar medium of our galaxy which can cause a rotation in the polarization position angle. It also does not include scattering of continuum photons in to resonance with emission lines which can change the polarization position angle if the geometry of the continuum scattering region is different from that of the emission line scattering region. One common feature both in our data, best seen in SDSSJ1652+1728E, as well as many SNe (Wang & Wheeler 2008) is the presence of loops in the Q/U plane where both the amount of polarization and the polarization position angle varies across the emission line, representing a large physical deviation from axial symmetry. Possible explanations for loops in the Q/U plane include an overall asymmetry to the scattering structure, an additional expanding shell with a different geometry, or the breakup of an axially-symmetric scattering structure into clumps (Kasen et al. 2003; Wang & Wheeler 2008).

Loops in the Q/U plane as a function of wavelength across emission lines has been widely observed among a number of AGN observed with spectropolarimetry. Smith et al. (1995) argued that structure in the polarization fraction of the emission lines in Mrk 231 requires several scattering components. Smith et al. (2000) further argued that structure in the polarization fraction and polarization position angle across broad emission lines coupled with larger values of polarization in the continuum than the emission lines implies that the the BLR of the 2MASS quasars contains multiple scattering components. In contrast, Young (2000), Smith et al. (2005), and Young et al. (2007) have argued that such swings in the polarization position angle are due to emission and scattering by an equatorial disk wind that is visible in Type 1 quasars but is overwhelmed by polar scattering signatures in Type 2 quasars.

4. DISCUSSION

Several trends are visible in our observations as noted in section 3:

1. polarization reaching $> 15\%$ in the continuum for three of five sources;
2. a ratio of emission line polarization/ continuum polarization that is close to 1/3 for ERQs and 4/5 in our Type 2 sources;
3. strong evidence for wavelength-dependent polarization fraction in the emission lines; and
4. change in the polarization position angle across emission lines of $\sim \pi/2$ radians, with the redshifted line emission at the same position angle as the continuum.

4.1. *Proposed Model*

To model these trends, we vary a number of parameters. Polarimetry models include both an emission and scattering region (though they can be coincident) which can be either stationary or have some velocity. In addition, we can vary the type of scatterer and scattering mechanism. For example, the classical model that explains the spectropolarimetry of obscured quasars is that of a point-like emitting region with a conical scattering region defined by the opening angle of the torus (Miller et al. 1991).

Combining all of these considerations, we constructed a model of the emission, scattering and resulting polarization expected for simple geometries and polarization mechanisms. The full details of this model are available in Zakamska et al. 2017 (in prep). We find that the model with the best fit to our data is a polar emission region (expanding emission within a filled cone) which is scattered by dust in an equatorial outflow (see Figure 6). While there are certainly more complicated geometries that would reproduce all our results, this model has the advantage of being straightforward and physically motivated.

There is both observational evidence and much theoretical work to support an equatorial, dusty outflow from the AGN torus that is supported by radiation pressure

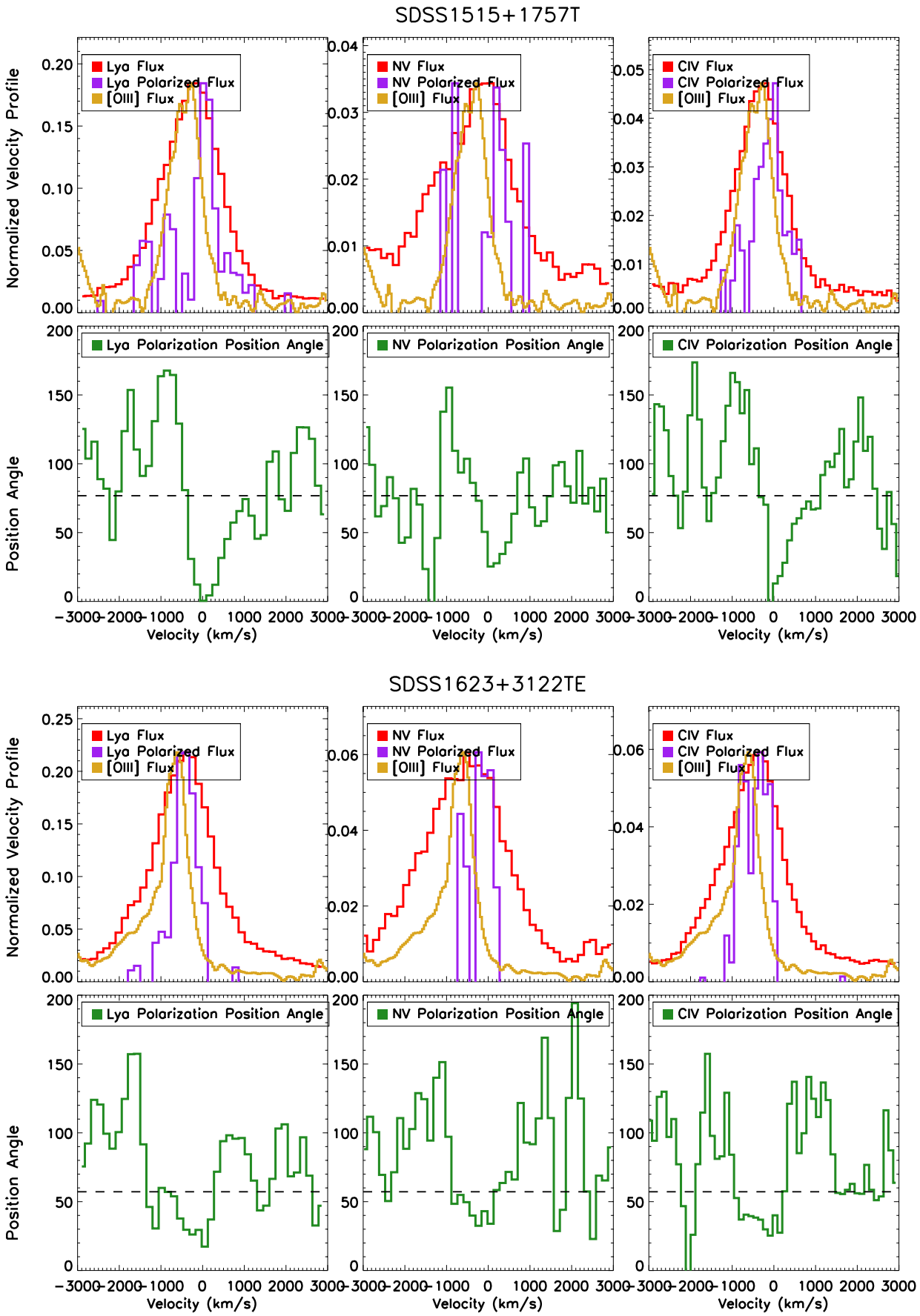

Figure 4. : LRISp spectrum of SDSSJ1515+1757T, SDSSJ1623+3122TE, and SDSSJ1652+1728E over various important emission line regions in velocity space. We overplot the total flux of the line (red), the polarized flux (polarization fraction × flux; purple), and the [OIII] flux (yellow), all scaled to arbitrary units to illustrate how the different quantities exhibit various structures in velocity space. We also show the polarization position angle (green) below.

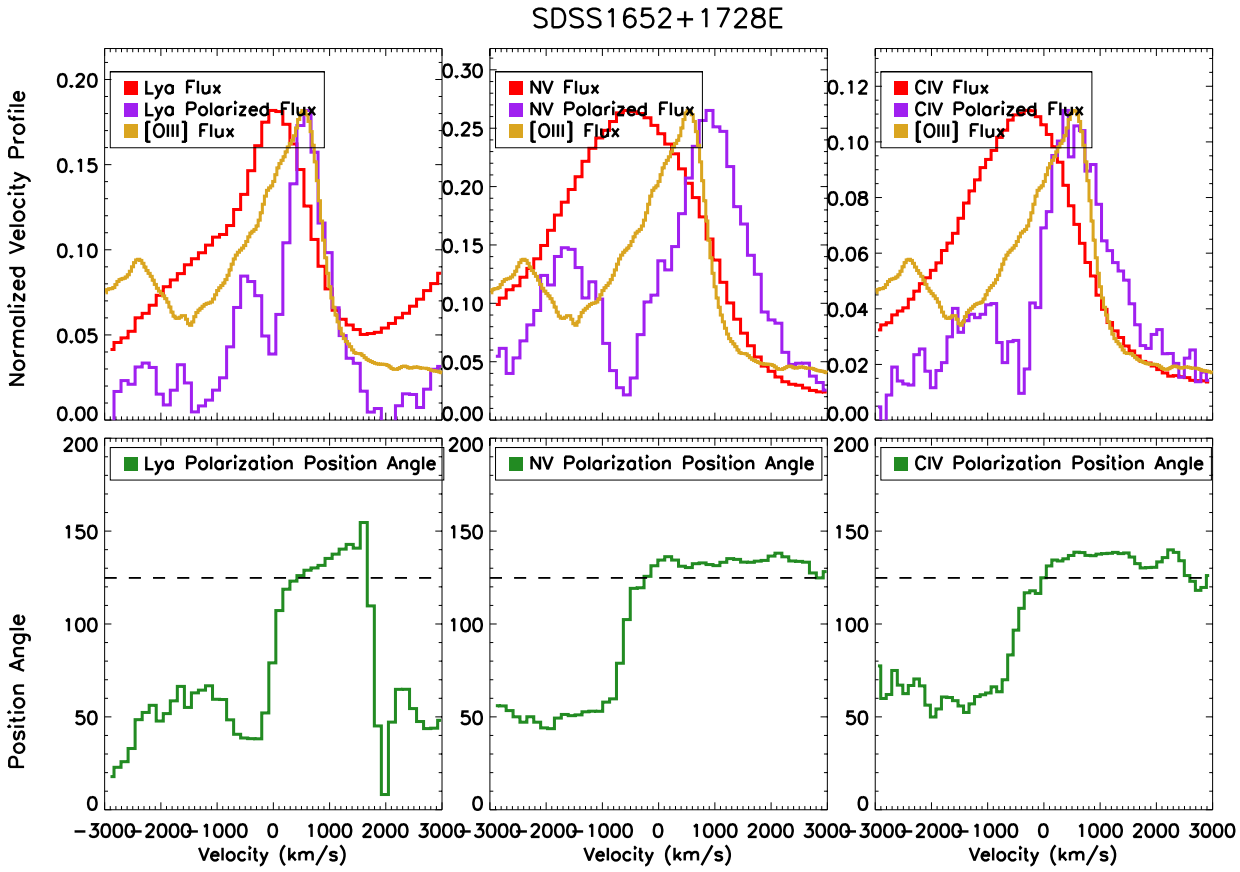

Figure 4. : continued

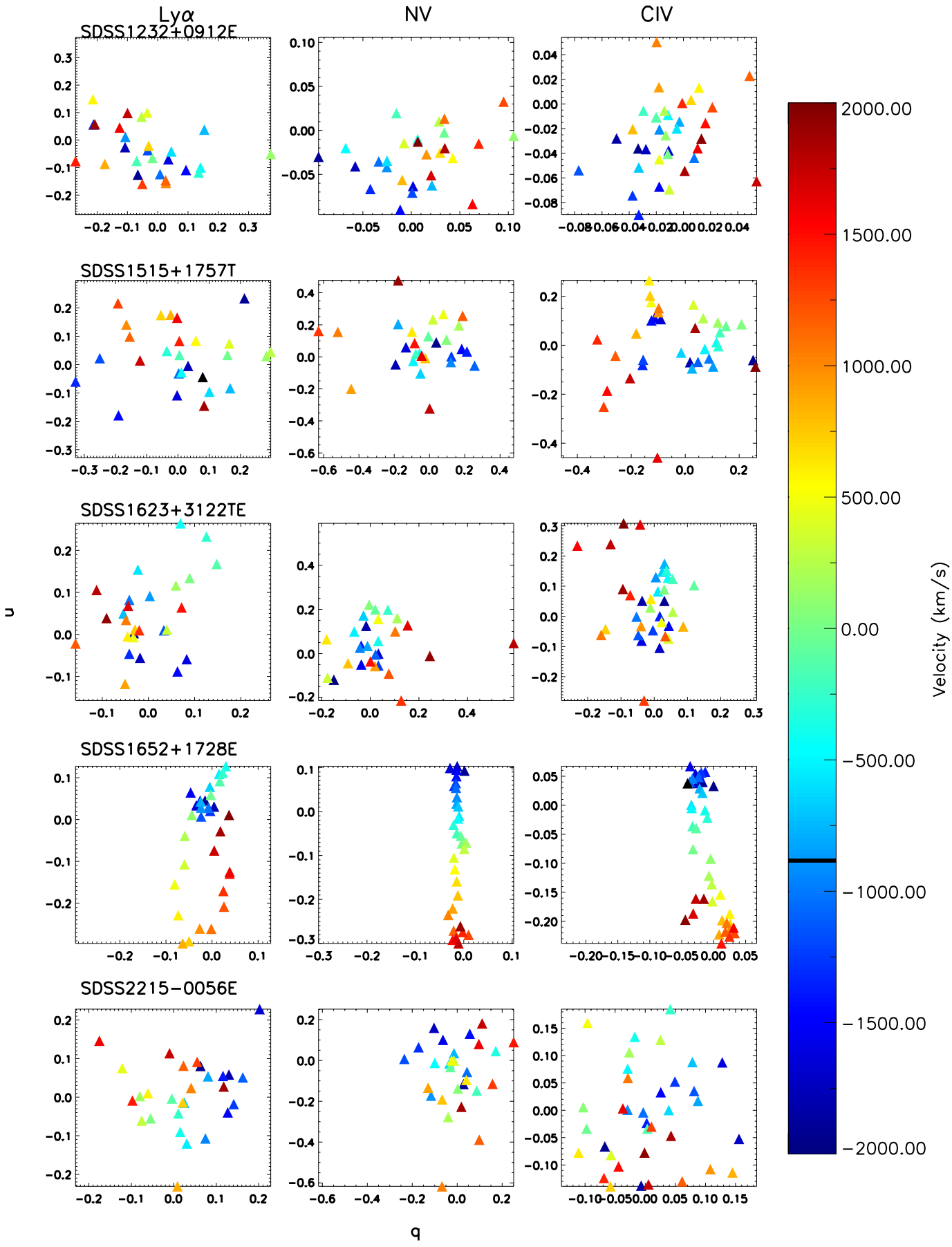

Figure 5. : Plot of q and q Stokes parameters for each of the key emission lines in our targets. Each point represents a spectroscopic pixel. We show over ±2000 km s^{-1} in velocity space with the colour scale. Notice, especially in SDSSJ1652+1728E, the clear presence of loops in q vs. u space.

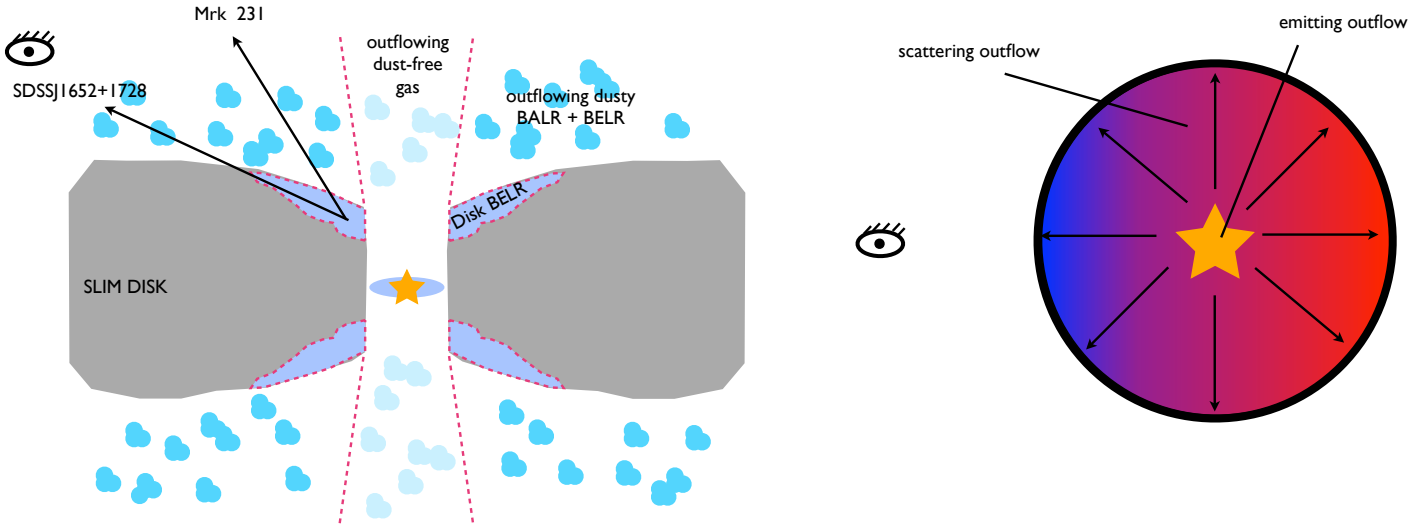

Figure 6. : Our preferred model for SDSSJ1652+1728 is adapted from Veilleux et al. (2016). It combines a polar outflow which produces the emission lines with a dusty equatorial wind where the scattering occurs. **Left:** Side-on view of the inner ∼10 pc of our model (not to scale). The inner accretion disk ($\lesssim$ 0.01pc) is responsible for the X-ray emission and is surrounded by a geometrically-thick accretion disk ("slim disk") which, for a near- or super-Eddington quasar produces narrow funnels that drive a polar wind. This polar wind is comprised of both dust-free outflowing gas, responsible for X-ray absorption, as well as dusty clouds that produce FeLoBAL absorption signatures and the blueshifted FUV emission lines of Lyα and C IV. The extended accretion disk is the source of the UV and optical continuum emission as well as the Balmer lines (seen through the screen of the outflowing dusty BALR). Mrk 231 is constrained to have a jet angle of $\theta_{max} = 25.6^{+3.2}_{-2.2}$ degrees from radio observations (Reynolds et al. 2013). This means that the scattered light, though still significant, is unpolarized in the observer's line of sight due to geometric cancellation. In contrast, SDSSJ1652+1728 is seen at a larger angle to the jet or polar axis as inferred from the mean SED of ERQs (see section 4.1 for further discussion). The increased column density of obscuration suppresses the FeLoBAL features while the more edge-on sight line reduces geometric cancellation of the polarization signature. Though the original cartoon contains a radio jet we omit this as it is not the subject of this work. **Right:** The same model as viewed from above (looking along the polar axis). Here we show how the kinematic features in the polarized emission-line regions are created by the blue and red-shifted scattering emission respectively. The viewer (eye on the left) sees blueshifted emission coming towards them and scattered off of cloudsmoving towards the observer. In contrast, the redshifted wings of the emission lines are dominated by scattering off the "sides" of the outflow (from the observers perspective). Emission from the back of the cone is largely suppressed in polarization because the scattering efficiency is low at angles $\gtrsim$ 90 degrees though this emission does contribute to the overall redshift of polarized emission lines compared to the unpolarized emission lines. These features combined produce the ninety degree rotation in the polarization position angle across the emission lines.

(e.g. Wills et al. 1992; Elitzur & Shlosman 2006; Veilleux et al. 2016; Chan & Krolik 2016; Elvis 2017). If the AGN is near or super-Eddington, the creation of a geometrically thick accretion flow also produces polar radiation driven outflows (e.g. Abramowicz et al. 1988; Sądowski et al. 2015; McKinney et al. 2015). We adapt the cartoon of Veilleux et al. (2016) who model Mrk 231 with a slim disk responsible for the continuum emission. The broad emission line region (BELR) is composed of a polar region, an extended accretion disk atmosphere and the disk itself (see Veilleux et al. 2016, figure 8 and our Figure 6) whereas the broad absorption line region (BALR) originates only in the polar outflow and disk atmosphere. Using this model, the FeLoBAL features are produced in the BALR, blueshifted FUV emission lines are produced in the outflowing BELR, and the optical and NUV emission lines are produced in the disk BELR. We find that some of the features of this model reproduce well our spectropolarimetry results. In particular, when the FUV lines are produced in the polar region and then are scattered by a dusty, ionized equatorial outflow, the puzzling kinematics of the emission lines can be reproduced.

The main difference between Mrk231 and our objects (ERQs and Type 2s) is that our viewing angle is closer to edge-on than the $\sim$ 25 degrees polar viewing angle inferred for Mrk 231 from radio observations (Reynolds et al. 2013). We make this conclusion on the basis of the shape of the SED of our sources (Zakamska et al. 2016; Hamann et al. 2017): as a function of wavelength, ERQ SEDs do not rise until 1-2μm, whereas Mrk231 is essentially unobscured at Hα wavelengths in the optical, and the steep rise of the Mrk 231 SED occurs at $\sim$ 3000Å. Therefore, the net line-of-sight column density of obscuration is $\sim$ 10 times higher in ERQs than in Mrk 231, implying the more edge-on viewing angle. For an SMC-like dust curve (Weingartner & Draine 2001; Draine 2003) in the "screen of cold dust" approximation, the Mrk231 rise would correspond to $A_{\rm V} \simeq 0.3$ mag, and the $1-2\mu$m rise for ERQs would correspond to $A_{\rm V} \simeq 5$ mag. This difference in viewing angle could explain why Mrk 231 exhibits low levels of FUV polarization – at the viewing angle of Mrk 231 the scattering region becomes nearly symmetric and thus geometric cancellation would dilute the polarization fraction (similar polarization fractions with opposite scattering angles will combine to produce a lower total polarization fraction) though the scattered flux is still high.

In subsequent sections we explore how this model matches the observational trends noted in our data. Section § 4.2 explains how this model matches our continuum polarization results while Section § 4.3 shows how this model produces the expected line polarization features. Finally, in § 4.4 we demonstrate that resonant scattering does not have a significant impact on our preferred model.

4.2. *Continuum Polarization and Scattering Geometry*

While scattering off of dust or electrons is the most likely source of polarization in AGN, especially at the high levels we observe in our objects, without some understanding from imaging of the scales on which polarization occurs it is difficult to distinguish between the two. For objects where the scattering cone is visible on $\sim$kpc scales (Dey et al. 1996; Kishimoto et al. 2001; Zakamska et al. 2005) the required gas mass for electron scattering is likely prohibitive though it is not always possible to completely rule out. In contrast, on circumnuclear scales the polarization of NGC 1068 is wavelength-independant from the X-ray to the optical, and is therefore likely due to electron scattering (Miller et al. 1991).

The high infrared-to-optical ratios and multiple features of the rest-frame optical spectra of our objects (Alexandroff et al. 2013; Ross et al. 2015; Zakamska et al. 2016; Hamann et al. 2017) indicate that they are obscured. We also know that the observed UV continuum of our objects is dominated by scattered light, because the net continuum polarization is so high that it cannot be appreciably diluted by the direct (unpolarized) light of the host galaxy. Therefore, scattering must be happening primarily on scales greater than obscuration scales, which in turn must be larger than the dust sublimation region (defined by the radius, $r_{\rm dust}$; Barvainis 1987, equation 5):

$$r_{\rm dust} = 1.3 \left(\frac{L_{\rm UV}}{10^{46}{\rm erg/sec}}\right)^{1/2} \left(\frac{T}{1500{\rm K}}\right)^{-2.8} {\rm pc}. \quad (1)$$

Here $L_{\rm UV}$ is the UV luminosity and T is the dust sublimation temperature. In the case of our extremely luminous sources ($L_{\rm UV} \approx$ a few $\times 10^{47}$), the sublimation scales might reach a few to 10 pc.

For a normal dust-to-gas ratio, the cross-section of dust scattering is two orders of magnitude higher than the electron scattering cross-section (Draine 2003), therefore since scattering must be happening outside of the dust sublimation zone, the presence of dust implies that dust scattering dominates our scattered light. In our proposed model, therefore, the dust scattering occurs somewhere in the BELR/BALR region (see Figure 6).

Scattering efficiency, the ratio of scattered flux to the flux that would have been observed directly in the absence of obscuration, is

$$\epsilon = \frac{{\rm d}\sigma}{{\rm d}\Omega} \Delta\Omega \int n_{\rm H}(r) {\rm d}r. \quad (2)$$

Here ${\rm d}\sigma/{\rm d}\Omega$ is the cross-section of scattering per unit hydrogen atom as calculated in Draine (2003), $\Delta\Omega$ is the solid angle covered by the scatterer as seen from the emitter, and $\int n_{\rm H}(r){\rm d}r$ is the column density of hydrogen associated with the scattering region. For a constant velocity outflow, $n_{\rm H}(r) \propto 1/r^2$, and therefore this integral is weighted toward the smallest unobscured sizes, so it is $\sim n_{\rm H,max} d_{\rm min}$. We take a fiducial value of $\epsilon = 3\%$, which is obtained by extrapolating the IR emission of ERQs using a type 1 quasar SED (Richards et al. 2006) toward UV wavelengths to see what fraction of this estimated intrinsic emission is observed (see figure 16 and figure 8 of Zakamska et al. 2016 Hamann et al. 2017, respectively). We take $\Delta\Omega = \frac{4\pi}{3}$ and 90° scattering by SMC dust with ${\rm d}\sigma/{\rm d}\Omega \simeq 4 \times 10^{-24}$ cm^2/H/Ω at 1500Å(Draine 2003). We arrive at the constraint in Figure 7 and hydrogen densities for scattering material on the order of $10 - 100$ cm^{-3}.

If this scattering region is too dusty, then no emission from the quasar could escape at all. Therefore, we need to verify that our derived densities and sizes are compatible with the escape of radiation from the quasar in order

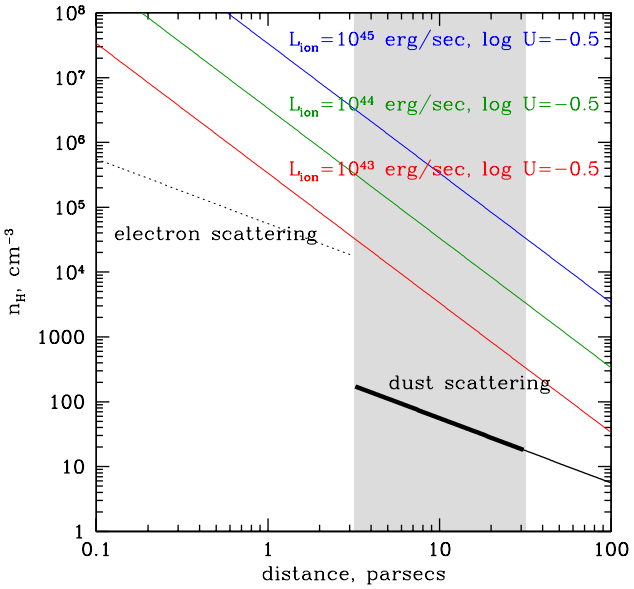

Figure 7. : The scattering efficiency and ionization parameter allow us to place constraints on the size of the scattering region and the density of scattering material. Assuming a scattering efficiency of 3% and following from equation 3, the black lines show the range of densities for reasonable distances to the dust (solid) or electron (dotted) scattering regions respectively. The coloured lines in the upper right show the limits on the density placed at the same distances based on our assumptions of the quasar ionizing luminosity and ionization parameter (see equation 4. Our preferred regime is the grey region which covers dust scattering at scales 3-30 pc (around the dust sublimation radius) though we are not able to place strong limits on the actual ionizing luminosity available from our quasars which is likely suppressed by extinction. We hypothesize that these two limits are incompatible because while the line emission is occurring in dense clouds in the quasar BELR, the scattering is occurring on similar scales but in the less dense medium surrounding these clouds.

to be available for scattering into our line of sight. We use equation 2 to find the optical depth to dust extinction through the scattering region:

$$\tau = C_{\rm ext} \int n_{\rm H} {\rm d}r = \frac{\epsilon C_{\rm ext}}{\Delta\Omega {\rm d}\sigma/{\rm d}\Omega}, \quad (3)$$

where $C_{\rm ext} = 2.9\times10^{-22}$ cm^2/H is the total cross-section for extinction (Weingartner & Draine 2001). With our fiducial values, $\tau \simeq 0.5$ and is therefore just right: a quasar viewed through BELR / BALR would be reddened, as is Mrk 231, but not completely extinguished. We also see from this expression that the scattering efficiency, ϵ, cannot be a lot greater than our fiducial value, because otherwise the extinction becomes prohibitively high. Therefore we conclude that our observed scattered component cannot be appreciably extincted or obscured, either by diffuse or by patchy material.

Assuming an SMC-like dust distribution, the theoretically achievable maximum polarization fraction at 1800 Å is $\sim 14.7\%$ for a scattering angle of 90° and the polarization fraction continues to rise towards the blue (Draine 2003). Thus, some of our targets display such high levels of polarization in the continuum that they come close to reaching this theoretically achievable limit and the geometric cancellation of polarization means that to achieve the observed 15% polarization level, the intrinsic polarization level of each scattering must be even higher. We know dust can be an efficient polarizer depending on the size distribution of the dust as compared to the wavelength of the scattered light (Weingartner & Draine 2001). Thus, to achieve the observed polarization fraction in our sources might require some adjustments to the dust size distribution compared to pre-existing models. The same is true for any wavelength-dependence in the polarization fraction of our objects that appears to increase towards redder wavelengths– in contrast to the Draine (2003) predictions. It is also not possible at this time to rule out a wavelength-dependent unpolarized component which dilutes the polarization as the cause of any wavelength-dependent polarization signatures in our continuum data.

4.3. *Line Polarization*

In low-redshift type 2 quasars, scattering occurs on a wide range of scales reaching several kpc (Hines et al. 1999; Zakamska et al. 2005, 2006; Schmidt et al. 2007; Obied et al. 2016) and on the same scales as the optical forbidden lines such as [O III] are produced. The co-spatial distribution of the line-emitting gas and of the scattering medium leads to a geometric cancellation of the polarization of the emission lines and to mixing of direct (unpolarized) emission with scattered light, resulting in the observed low fractional polarization of the narrow emission-line region (Stockman et al. 1981; Glenn et al. 1994; Goodrich & Miller 1995; Tran 1995).

In our objects, we observe a lower net polarization of the UV emission lines than in the continuum. By analogy to the suppression of polarization of the narrow-line region of type 2 quasars, we hypothesize that the UV emission lines arise on scales similar to those that dominate scattering. In the cartoon shown in Figure 6, the low fractional polarization of the emission lines would be achieved if the lines are produced either in the dusty BELR / BALR or in the dust-free cone at scales similar to or greater than the scales of the dusty BELR / BALR. There is also empirical evidence (Czerny & Hryniewicz 2011) and emission line calculations (Netzer & Laor 1993) that suggest the broad-liner region and inner edge of the obscuring material should exist on similar scales.

In the simple case of a spherical emitting region of radius R and scattering region of radius D, Cassinelli et al. (1987) show that the polarization is reduced by a factor of $[1-(R/D)^2]^{1/2}$ relative to an emitting point source. If we assume that the continuum emitting region is a point source, and it is roughly $\sim 3\times$ more polarized than the emission line region, this implies that the emission line region is 94% the size of the scattering region, confirming that the emission line region and scattering regions extend to similar scales.

What constraints on the physical conditions do we get from requiring that continuum scattering and UV emission line production occur on similar scales? The ionization parameter is

$$U = \frac{L_{\rm ion}}{4\pi r^2 \phi n_e c}. \quad (4)$$

Here $L_{\rm ion}$ is the luminosity of the ionizing radiation, $\phi =$ 13.6 eV is the threshold energy of the ionizing photons, and $n_e \simeq (1-1.2) \times n_{\rm H}$ is the electron density which depends slightly on whether helium is fully ionized. As a fiducial value of the ionization parameter in the C IV-emitting region we use $\log U = -0.5$ from Rodríguez Hidalgo et al. (2011).

It is clear from Figure 7 that if emission lines are produced on spatial scales that are similar to those of scattering, then either a strong suppression of the ionizing continuum or strong clumping of the emission-line gas or both are required to produce the observed ionization parameter. We will model the UV emission lines of ERQs in a forthcoming photo-ionization analysis of the emission line ratios (Hamann et al., in prep.). In the meanwhile, our qualitative model is that the emission lines are produced in high density clouds either in the joint BELR / BALR or in the dust-free zone. These clouds are ionization-bounded and therefore are by definition optically thick to ionizing radiation, so only the compact surfaces of these clouds will be able to scatter continuum emission in the dusty zone (scattering is much weaker in the dust-free zone and is unlikely to dominate). Thus, scattering is dominated by a lower-density, volume-filling component of the BELR / BALR gas. This allows us to reconcile the densities implied by the scattering efficiency and by the ionization parameter (see Figure 7).

The biggest success of our model in Figure 6 is that our model naturally explains the change in the polarization fraction and position angle as a function of velocity in the FUV emission lines. The blue-shifted line emission we see in our objects is from the near-side of the equatorial outflow which gives it the observed velocity shift (see the right panel of Figure 6). In contrast, the observed redshifted emission is dominated not by the back of the outflow (this emission is suppressed because dust back scattering is inefficient) but instead from the sides of the equatorial outflow which are moving away from the observer and thus produce redshifted scattered emission. This results in the swing in polarization position angle as a function of velocity in the emission lines as the two scattering regions are roughly perpendicular to each other as seen in the plane of the sky so the polarization position angle transitions as a function of velocity from being dominated by the near-side of the equatorial outflow in the blue to the sides of the outflow in the red. This also explains the overall redshift in emission line features seen in polarized light as the net redshift of the scattered line is due to the redshift of the scatterer relative to the emitter.

Smith et al. (2004) suggested a similar model of the torus with both polar and equatorial scattering regions to explain the range of properties observed in low redshift Seyfert 1s and 2s. The polar scatterer extends beyond the torus and may be outflowing while the equatorial scatterer lies within the torus and is described by Young (2000) as a rotating disk wind. Other differences between our model and Young (2000) model include the specific emission lines: they consider Balmer lines, which in our cartoon are produced in a more extended region of the disk than the FUV lines which we focus on. Furthermore, in Type 1 objects there is dilution of the scattered light by the direct unpolarized continuum, which may explain the much lower values of polarization and position angle swings achieved in Seyfert 1s. But the main difference is that Young (2000) explain the rotation in the polarization position angle using a rotating disk wind, where rotation might be difficult to maintain dynamically. In contrast, in our model the polarization position angle swing is achieved naturally by the geometric projection effects, with the blueshifted scattered emission and the redshifted scattered emission having different orientations in projection on the plane of the sky.

4.4. *Resonant Scattering?*

In addition to scattering by either electrons or dust grains, resonant scattering is a possible mechanism for the polarization observed in the emission lines of our objects. Permitted electric dipole transitions in an anisotropic radiation field can produce linearly polarized emission, and thus resonantly polarized scattering becomes important mechanism either if the emission line source region is not spherically symmetric, or if radiation, either from an emission line or the continuum region, is Doppler-shifted into resonance with a permitted transition and is incident on a gas cloud (Lee & Blandford 1997). For a single $\Delta J = 0-1$ scattering viewed at 90 degrees the polarization reaches 100% (Hamilton 1947). However, the resonant scattering in AGNs might involve multiple scatterings, and if the optical depth to scattering is high enough the net expected polarization signal is low. Lee (1994) showed that standard emission-line clouds emit almost completely unpolarized line radiation unless the optical depth is $\tau \lesssim 1$ which is usually only the case for the semi-forbidden C III] λ1909 transition. For reflection off of nearby clouds to contribute significantly to the polarized line emission the optical depth must be in a specific regime where only a small number of reflections occur. Lee & Blandford (1997) determine that this happens at a column density of $N \sim 10^{17}$ cm^{-2} for a single reflection which is approximately six orders of magnitude smaller than the regime where electron scattering has a significant effect ($N \sim 10^{23}$ cm^{-2}). We will find that resonant scattering contributes at most only modestly to the polarization fraction in our objects.

We can calculate the expected ratio of the optical depth of resonant scattering compared to the optical depth to dust scattering. The optical depth to dust scattering, τ_{dust} is given by

$$\tau_{dust} = N_H \times C_{ext,H} \tag{5}$$

assuming a constant number density of dust grains along the line of sight. Here N_H is the column density of hydrogen nucleons and $C_{ext,H}$ is the extinction cross section of the dust per hydrogen nucleon, taken to be 3.768×10^{-22} cm^2/H for an SMC-like dust distribution at 1200Å from Draine (2003). Similarly, the optical depth to resonant scattering, τ_{res} is given by:

$$\tau_{res} = N_H \times \frac{m_C}{m_H} \frac{\Delta v}{v_{wind}} \sigma_{res} \tag{6}$$

where $\frac{m_C}{m_H} \simeq 1.0 \times 10^{-3}$ is the mass ratio of C IV to H nucleons which we estimate based on the assumption that the number ratio of carbon to hydrogen in the ISM is solar, $\frac{\log N_H}{\log N_C} = 3.57$ (Grevesse et al. 2010), and $\sim 30\%$

of carbon is triply ionized (Proga, personal communication). $\frac{\Delta v}{v_{wind}} \approx 0.1$ is the fraction of photons that lie within a thermal width of the resonance frequency given an estimate of the outflow velocity of $v_{wind} \approx 3000$ km s^{-1} and the gas temperature $T \approx 15,000$K based on the assumption of photo-electric temperature balance C IV. Finally, the cross section for resonant scattering is taken to be $\sim 1.0 \times 10^{-17}$ cm^2 for a single scattering event as taken from Lee et al. (1994). Combining these quantities gives us a rough estimate for the ratio of the dust scattering to resonant scattering optical depth of $\frac{\tau_{res}}{\tau_{dust}} \approx 0.3$ implying that resonant scattering in the emission lines of our objects is likely present but at most enhances the polarization fraction by $\sim 30\%$. We thus conclude that continuum dust scattering is the dominant scattering mechanism both for the continuum and the emission lines.

5. CONCLUSIONS

We have obtained rest-frame ultraviolet spectropolarimetry for five $z \sim 2.5$ obscured and highly reddened quasars using LRIS in polarimetry mode on Keck. Our Type 2 targets are classically selected, narrow-line objects (Alexandroff et al. 2013). Extremely red quasars are color-selected and show signs of extreme outflow activity in their rest-frame optical spectra (Ross et al. 2015; Zakamska et al. 2016; Hamann et al. 2017). Although our initial expectations were that narrow line-selected Type 2s should be more highly polarized than the extremely red quasars, we find (in this admittedly small sample) no systematic trends between the optical and UV "type" and the levels of continuum polarization.

We do see several interesting trends in our polarization data:

1. We find high levels of polarization in the continuum, higher than 15% in three of our sources, with some signs that the polarization fraction may be increasing to longer wavelengths.

2. We find lower levels of polarization in emission lines with a ratio of continuum polarization/emission line polarization between 1/3 and 4/5.

3. Intriguingly, we see a rotation of almost exactly ninety degrees in the polarization position angle across all strong emission lines, Lyα, CIV, and NV;

4. The polarization position angle of the continuum matches the polarization position angle at the most redshifted part of emission lines.

To explain our data, we prefer a model in which an equatorial dusty disk wind scatters both continuum emission from the disk and line emission from a polar outflow. This model is physically motivated and appears to match the main features of our observations. The high polarization fraction can be explained by dust scattering though it may require a few adjustments to typical dust models. Assuming the emission line region and dusty scattering region exist on similar scales that are larger than the continuum emission region produces the lower polarization fraction observed in the emission lines of our objects. Finally, this model allows for different outflow components to dominate in the continuum and the red wavelengths of emission lines compared to the blue wavelengths of emission lines and thus produces a ninety degree rotation in the polarization position angle as a function of wavelength across the emission lines as observed.

Absent high resolution imaging, spectropolarimetry can be an important tool to understand the scattering geometry of our high redshift obscured and reddened quasars and can be an important piece of information to evaluate different proposed models of quasar geometry on small scales near the black hole. This allows us a window in to the potential launching mechanism for galaxy-scale quasar winds which are a necessary ingredient for quasar feedback.

The data presented herein were obtained at the W.M. Keck Observatory, which is operated as a scientific partnership among the California Institute of Technology, the University of California and the National Aeronautics and Space Administration. The Observatory was made possible by the generous financial support of the W.M. Keck Foundation. The authors wish to recognize and acknowledge the very significant cultural role and reverence that the summit of Mauna Kea has always had within the indigenous Hawaiian community. We are most fortunate to have the opportunity to conduct observations from this mountain.

R.A. was supported in part by NASA JPL grant 1520456. Support for this work was provided in part by the National Aeronautics and Space Administration through Chandra Award Number GO6-17100X issued by the Chandra X-ray Observatory Center, which is operated by the Smithsonian Astrophysical Observatory for and on behalf of the National Aeronautics Space Administration under contract NAS8-03060. R.A. would like to acknowledge the assistance of C. Steidel, A. Strom, D. Perley, and H. Tran during observations at Keck I and the assistance of M. Kassis on the evening of LRISp observations. R. A. would also like to thank D. Neufeld for his useful conversations and S. Veilleux for allowing us to adapt figure 8 of Veilleux et al. 2016. N. L. Z. would like to acknowledge the remote observing support of Yale University and support by the Catalyst award of the Johns Hopkins University.

REFERENCES

Abramowicz, M. A., Czerny, B., Lasota, J. P., & Szuszkiewicz, E. 1988, ApJ, 332, 646
Ahn, C. P., Alexandroff, R., Allende Prieto, C., Anderson, S. F., Anderton, T., Andrews, B. H., Aubourg, É., Bailey, S., Balbinot, E., Barnes, R., & et al. 2012, ApJS, 203, 21
Alexandroff, R., Strauss, M. A., Greene, J. E., Zakamska, N. L., Ross, N. P., Brandt, W. N., Liu, G., Smith, P. S., Ge, J., Hamann, F., Myers, A. D., Petitjean, P., Schneider, D. P., Yesuf, H., & York, D. G. 2013, MNRAS, 435, 3306
Antonucci, R. 1993, ARA&A, 31, 473
Antonucci, R. R. J. & Miller, J. S. 1985, ApJ, 297, 621
Assef, R. J., Walton, D. J., Brightman, M., Stern, D., Alexander, D., Bauer, F., Blain, A. W., Diaz-Santos, T., Eisenhardt, P. R. M., Finkelstein, S. L., Hickox, R. C., Tsai, C.-W., & Wu, J. W. 2016, ApJ, 819, 111
Banerji, M., Alaghband-Zadeh, S., Hewett, P. C., & McMahon, R. G. 2015, MNRAS, 447, 3368
Barth, A. J., Filippenko, A. V., & Moran, E. C. 1999, ApJ, 525, 673
Barvainis, R. 1987, ApJ, 320, 537

Berriman, G., Schmidt, G. D., West, S. C., & Stockman, H. S. 1990, ApJS, 74, 869
Borguet, B., Hutsemékers, D., Letawe, G., Letawe, Y., & Magain, P. 2008, A&A, 478, 321
Cassinelli, J. P., Nordsieck, K. H., & Murison, M. A. 1987, ApJ, 317, 290
Chan, C.-H. & Krolik, J. H. 2016, ApJ, 825, 67
Czerny, B. & Hryniewicz, K. 2011, A&A, 525, L8
Dawson, K. S., Schlegel, D. J., Ahn, C. P., Anderson, S. F., Aubourg, É., Bailey, S., Barkhouser, R. H., Bautista, J. E., Beifiori, A., Berlind, A. A., & et al. 2013, AJ, 145, 10
Dey, A., Cimatti, A., van Breugel, W., Antonucci, R., & Spinrad, H. 1996, ApJ, 465, 157
Donley, J. L., Koekemoer, A. M., Brusa, M., Capak, P., Cardamone, C. N., Civano, F., Ilbert, O., Impey, C. D., Kartaltepe, J. S., Miyaji, T., Salvato, M., Sanders, D. B., Trump, J. R., & Zamorani, G. 2012, ApJ, 748, 142
Draine, B. T. 2003, ApJ, 598, 1017
Eisenhardt, P. R. M., Wu, J., Tsai, C.-W., Assef, R., Benford, D., Blain, A., Bridge, C., Condon, J. J., Cushing, M. C., Cutri, R., Evans, II, N. J., Gelino, C., Griffith, R. L., Grillmair, C. J., Jarrett, T., Lonsdale, C. J., Masci, F. J., Mason, B. S., Petty, S., Sayers, J., Stanford, S. A., Stern, D., Wright, E. L., & Yan, L. 2012, ApJ, 755, 173
Elitzur, M. & Shlosman, I. 2006, ApJL, 648, L101
Elvis, M. 2017, ArXiv e-prints
Glenn, J., Schmidt, G. D., & Foltz, C. B. 1994, ApJL, 434, L47
Glikman, E., Helfand, D. J., White, R. L., Becker, R. H., Gregg, M. D., & Lacy, M. 2007, ApJ, 667, 673
Glikman, E., Simmons, B., Mailly, M., Schawinski, K., Urry, C. M., & Lacy, M. 2015, ApJ, 806, 218
Glikman, E., Urrutia, T., Lacy, M., Djorgovski, S. G., Mahabal, A., Myers, A. D., Ross, N. P., Petitjean, P., Ge, J., Schneider, D. P., & York, D. G. 2012, ApJ, 757, 51
Glikman, E., Urrutia, T., Lacy, M., Djorgovski, S. G., Urry, M., Croom, S., Schneider, D. P., Mahabal, A., Graham, M., & Ge, J. 2013, ApJ, 778, 127
Goodrich, R. W., Cohen, M. H., & Putney, A. 1995, PASP, 107, 179
Goodrich, R. W. & Miller, J. S. 1995, ApJL, 448, L73
Greene, J. E., Alexandroff, R., Strauss, M. A., Zakamska, N. L., Lang, D., Liu, G., Pattarakijwanich, P., Hamann, F., Ross, N. P., Myers, A. D., Brandt, W. N., York, D., & Schneider, D. P. 2014, ApJ, 788, 91
Grevesse, N., Asplund, M., Sauval, A. J., & Scott, P. 2010, Ap&SS, 328, 179
Hamann, F., Zakamska, N. L., Ross, N., Paris, I., Alexandroff, R. M., Villforth, C., Richards, G. T., Herbst, H., Brandt, W. N., Cook, B., Denney, K. D., Greene, J. E., Schneider, D. P., & Strauss, M. A. 2017, MNRAS, 464, 3431
Hamilton, D. R. 1947, ApJ, 106, 457
Hao, L., Strauss, M. A., Tremonti, C. A., Schlegel, D. J., Heckman, T. M., Kauffmann, G., Blanton, M. R., Fan, X., Gunn, J. E., Hall, P. B., Ivezić, Ž., Knapp, G. R., Krolik, J. H., Lupton, R. H., Richards, G. T., Schneider, D. P., Strateva, I. V., Zakamska, N. L., Brinkmann, J., Brunner, R. J., & Szokoly, G. P. 2005, AJ, 129, 1783
Hines, D. C., Schmidt, G. D., Smith, P. S., Cutri, R. M., & Low, F. J. 1995, ApJL, 450, L1
Hines, D. C., Schmidt, G. D., Wills, B. J., Smith, P. S., & Sowinski, L. G. 1999, ApJ, 512, 145
Hoeflich, P., Wheeler, J. C., Hines, D. C., & Trammell, S. R. 1996, ApJ, 459, 307
Hopkins, P. F., Hernquist, L., Cox, T. J., Di Matteo, T., Robertson, B., & Springel, V. 2006, ApJS, 163, 1
Horne, K. 1986, PASP, 98, 609
Kasen, D., Nugent, P., Wang, L., Howell, D. A., Wheeler, J. C., Höflich, P., Baade, D., Baron, E., & Hauschildt, P. H. 2003, ApJ, 593, 788
Kauffmann, G., Heckman, T. M., Tremonti, C., Brinchmann, J., Charlot, S., White, S. D. M., Ridgway, S. E., Brinkmann, J., Fukugita, M., Hall, P. B., Ivezić, Ž., Richards, G. T., & Schneider, D. P. 2003, MNRAS, 346, 1055
Kishimoto, M., Antonucci, R., Cimatti, A., Hurt, T., Dey, A., van Breugel, W., & Spinrad, H. 2001, ApJ, 547, 667
Lee, H. W. 1994, MNRAS, 268, 49
Lee, H.-W. & Blandford, R. D. 1997, MNRAS, 288, 19
Lee, H.-W., Blandford, R. D., & Western, L. 1994, MNRAS, 267, 303
Mason, R. E., Rodríguez-Ardila, A., Martins, L., Riffel, R., González Martín, O., Ramos Almeida, C., Ruschel Dutra, D., Ho, L. C., Thanjavur, K., Flohic, H., Alonso-Herrero, A., Lira, P., McDermid, R., Riffel, R. A., Schiavon, R. P., Winge, C., Hoenig, M. D., & Perlman, E. 2015, ApJS, 217, 13
McKinney, J. C., Dai, L., & Avara, M. J. 2015, MNRAS, 454, L6
Miller, J. S. & Goodrich, R. W. 1990, ApJ, 355, 456
Miller, J. S., Goodrich, R. W., & Mathews, W. G. 1991, ApJ, 378, 47
Miller, J. S., Robinson, L. B., & Goodrich, R. W. 1988, in Instrumentation for Ground-Based Optical Astronomy, ed. L. B. Robinson, 157
Netzer, H. & Laor, A. 1993, ApJL, 404, L51
Norman, C., Hasinger, G., Giacconi, R., Gilli, R., Kewley, L., Nonino, M., Rosati, P., Szokoly, G., Tozzi, P., Wang, J., Zheng, W., Zirm, A., Bergeron, J., Gilmozzi, R., Grogin, N., Koekemoer, A., & Schreier, E. 2002, ApJ, 571, 218
Obied, G., Zakamska, N. L., Wylezalek, D., & Liu, G. 2016, MNRAS, 456, 2861
Oke, J. B., Cohen, J. G., Carr, M., Cromer, J., Dingizian, A., Harris, F. H., Labrecque, S., Lucinio, R., Schaal, W., Epps, H., & Miller, J. 1995, PASP, 107, 375
Reyes, R., Zakamska, N. L., Strauss, M. A., Green, J., Krolik, J. H., Shen, Y., Richards, G. T., Anderson, S. F., & Schneider, D. P. 2008, AJ, 136, 2373
Reynolds, C., Punsly, B., O'Dea, C. P., & Hurley-Walker, N. 2013, ApJL, 776, L21
Richards, G. T., Lacy, M., Storrie-Lombardi, L. J., Hall, P. B., Gallagher, S. C., Hines, D. C., Fan, X., Papovich, C., Vanden Berk, D. E., Trammell, G. B., Schneider, D. P., Vestergaard, M., York, D. G., Jester, S., Anderson, S. F., Budavári, T., & Szalay, A. S. 2006, ApJS, 166, 470
Rockosi, C., Stover, R., Kibrick, R., Lockwood, C., Peck, M., Cowley, D., Bolte, M., Adkins, S., Alcott, B., Allen, S. L., Brown, B., Cabak, G., Deich, W., Hilyard, D., Kassis, M., Lanclos, K., Lewis, J., Pfister, T., Phillips, A., Robinson, L., Saylor, M., Thompson, M., Ward, J., Wei, M., & Wright, C. 2010, in Proc. SPIE, Vol. 7735, Ground-based and Airborne Instrumentation for Astronomy III, 77350R
Rodríguez Hidalgo, P., Hamann, F., & Hall, P. 2011, MNRAS, 411, 247
Ross, N. P., Hamann, F., Zakamska, N. L., Richards, G. T., Villforth, C., Strauss, M. A., Greene, J. E., Alexandroff, R., Brandt, W. N., Liu, G., Myers, A. D., Pâris, I., & Schneider, D. P. 2015, MNRAS, 453, 3932
Sanders, D. B., Soifer, B. T., Elias, J. H., Madore, B. F., Matthews, K., Neugebauer, G., & Scoville, N. Z. 1988, ApJ, 325, 74
Sądowski, A., Narayan, R., Tchekhovskoy, A., Abarca, D., Zhu, Y., & McKinney, J. C. 2015, MNRAS, 447, 49
Schlafly, E. F. & Finkbeiner, D. P. 2011, ApJ, 737, 103
Schlegel, D. J., Finkbeiner, D. P., & Davis, M. 1998, ApJ, 500, 525
Schmidt, G. D., Elston, R., & Lupie, O. L. 1992a, AJ, 104, 1563
Schmidt, G. D., Smith, P. S., Hines, D. C., Tremonti, C. A., & Low, F. J. 2007, ApJ, 666, 784
Schmidt, G. D., Stockman, H. S., & Smith, P. S. 1992b, ApJL, 398, L57
Serkowski, K., Mathewson, D. S., & Ford, V. L. 1975, ApJ, 196, 261
Smith, J. E., Robinson, A., Alexander, D. M., Young, S., Axon, D. J., & Corbett, E. A. 2004, MNRAS, 350, 140
Smith, J. E., Robinson, A., Young, S., Axon, D. J., & Corbett, E. A. 2005, MNRAS, 359, 846
Smith, P. S., Schmidt, G. D., Allen, R. G., & Angel, J. R. P. 1995, ApJ, 444, 146
Smith, P. S., Schmidt, G. D., Hines, D. C., Cutri, R. M., & Nelson, B. O. 2000, ApJL, 545, L19
—. 2002, ApJ, 569, 23
Smith, P. S., Schmidt, G. D., Hines, D. C., & Foltz, C. B. 2003, ApJ, 593, 676

Stern, D., Eisenhardt, P., Gorjian, V., Kochanek, C. S., Caldwell, N., Eisenstein, D., Brodwin, M., Brown, M. J. I., Cool, R., Dey, A., Green, P., Jannuzi, B. T., Murray, S. S., Pahre, M. A., & Willner, S. P. 2005, ApJ, 631, 163
Stern, D., Moran, E. C., Coil, A. L., Connolly, A., Davis, M., Dawson, S., Dey, A., Eisenhardt, P., Elston, R., Graham, J. R., Harrison, F., Helfand, D. J., Holden, B., Mao, P., Rosati, P., Spinrad, H., Stanford, S. A., Tozzi, P., & Wu, K. L. 2002, ApJ, 568, 71
Stockman, H. S., Hier, R. G., & Angel, J. R. P. 1981, ApJ, 243, 404
Tadhunter, C. 2005, in Astronomical Society of the Pacific Conference Series, Vol. 343, Astronomical Polarimetry: Current Status and Future Directions, ed. A. Adamson, C. Aspin, C. Davis, & T. Fujiyoshi, 457
Tran, H. D. 1995, ApJ, 440, 597
Tran, H. D., Cohen, M. H., & Goodrich, R. W. 1995, AJ, 110, 2597
Treister, E., Cardamone, C. N., Schawinski, K., Urry, C. M., Gawiser, E., Virani, S., Lira, P., Kartaltepe, J., Damen, M., Taylor, E. N., Le Floc'h, E., Justham, S., & Koekemoer, A. M. 2009, ApJ, 706, 535
Tsai, C.-W., Eisenhardt, P. R. M., Wu, J., Stern, D., Assef, R. J., Blain, A. W., Bridge, C. R., Benford, D. J., Cutri, R. M., Griffith, R. L., Jarrett, T. H., Lonsdale, C. J., Masci, F. J., Moustakas, L. A., Petty, S. M., Sayers, J., Stanford, S. A., Wright, E. L., Yan, L., Leisawitz, D. T., Liu, F., Mainzer, A. K., McLean, I. S., Padgett, D. L., Skrutskie, M. F., Gelino, C. R., Beichman, C. A., & Juneau, S. 2015, ApJ, 805, 90
Urrutia, T., Becker, R. H., White, R. L., Glikman, E., Lacy, M., Hodge, J., & Gregg, M. D. 2009, ApJ, 698, 1095
Urry, C. M. & Padovani, P. 1995, PASP, 107, 803
van Dokkum, P. G. 2001, PASP, 113, 1420
Veilleux, S., Melendez, M., Tripp, T. M., Hamann, F., & Rupke, D. S. N. 2016, ArXiv e-prints
Wang, L., Howell, D. A., Höflich, P., & Wheeler, J. C. 2001, ApJ, 550, 1030
Wang, L. & Wheeler, J. C. 2008, ARA&A, 46, 433
Weingartner, J. C. & Draine, B. T. 2001, ApJ, 548, 296
Wills, B. J., Wills, D., Evans, II, N. J., Natta, A., Thompson, K. L., Breger, M., & Sitko, M. L. 1992, ApJ, 400, 96
Wright, E. L., Eisenhardt, P. R. M., Mainzer, A. K., Ressler, M. E., Cutri, R. M., Jarrett, T., Kirkpatrick, J. D., Padgett, D., McMillan, R. S., Skrutskie, M., & et al. 2010, AJ, 140, 1868
Wu, J., Tsai, C.-W., Sayers, J., Benford, D., Bridge, C., Blain, A., Eisenhardt, P. R. M., Stern, D., Petty, S., Assef, R., Bussmann, S., Comerford, J. M., Cutri, R., Evans, II, N. J., Griffith, R., Jarrett, T., Lake, S., Lonsdale, C., Rho, J., Stanford, S. A., Weiner, B., Wright, E. L., & Yan, L. 2012, ApJ, 756, 96
Yèche, C., Petitjean, P., Rich, J., Aubourg, E., Busca, N., Hamilton, J.-C., Le Goff, J.-M., Paris, I., Peirani, S., Pichon, C., Rollinde, E., & Vargas-Magaña, M. 2010, A&A, 523, A14
Young, S. 2000, MNRAS, 312, 567
Young, S., Axon, D. J., Robinson, A., Hough, J. H., & Smith, J. E. 2007, Nature, 450, 74
Yuan, S., Strauss, M. A., & Zakamska, N. L. 2016, MNRAS, 462, 1603
Zakamska, N. L. & Greene, J. E. 2014, MNRAS, 442, 784
Zakamska, N. L., Hamann, F., Pâris, I., Brandt, W. N., Greene, J. E., Strauss, M. A., Villforth, C., Wylezalek, D., Alexandroff, R. M., & Ross, N. P. 2016, MNRAS, 459, 3144
Zakamska, N. L., Schmidt, G. D., Smith, P. S., Strauss, M. A., Krolik, J. H., Hall, P. B., Richards, G. T., Schneider, D. P., Brinkmann, J., & Szokoly, G. P. 2005, AJ, 129, 1212
Zakamska, N. L., Strauss, M. A., Krolik, J. H., Collinge, M. J., Hall, P. B., Hao, L., Heckman, T. M., Ivezić, Ž., Richards, G. T., Schlegel, D. J., Schneider, D. P., Strateva, I., Vanden Berk, D. E., Anderson, S. F., & Brinkmann, J. 2003, AJ, 126, 2125
Zakamska, N. L., Strauss, M. A., Krolik, J. H., Ridgway, S. E., Schmidt, G. D., Smith, P. S., Heckman, T. M., Schneider, D. P., Hao, L., & Brinkmann, J. 2006, AJ, 132, 1496